Universität Rostock Traditio et Innovatio

Resolving Laser Induced Plasma Dynamics by Time-Resolved Coherent Diffractive Imaging

Master-Arbeit
angefertigt am Institut für Physik
der Mathematisch-Naturwissenschaftlichen Fakultät
der Universität Rostock

von Tom Böttcher, geb. am 18. Juni 2001 in Crivitz

Betreuer und 1. Prüfer : Dr. F. Fennel, Universität Rostock
2. Prüfer: Prof. Dr. S. Lochbrunner, Universität Rostock

Rostock, 26. August 2024

Abstract

Ultrashort laser pulses have been used to machine a wide variety of materials, including metals, semiconductors and insulators. Knowledge of the influence of laser parameters such as the spatial, temporal, and spectral characteristics of the pulse structure on the ablation processes is crucial for the development of precision laser machining techniques.

In order to unravel the processes that lead to ablation, an experimental method for observing the plasma dynamics in gold foils with a thickness of 30 nm, excited by an intense femtosecond (fs) 800 nm pump pulse, is presented. The excited foil is imaged by a low-intensity fs-400 nm probe pulse with a variable pump probe time delay of up to 2 ns and the diffraction image is captured with a CMOS camera in the far field. By employing a phase retrieval algorithm, the time- and space-resolved complex transmission is reconstructed from the captured diffraction images and knowledge about the plasma dynamics in the excited foil is extracted.

In this work, the impact of laser parameters, including the pump energy and polarization, on the plasma dynamics is examined. A decrease of transmission with increasing pump energy was observed in the first 10 ps and attributed to an increase of the free electron density due to the absorption of the pulse energy by the electrons. Furthermore, the onset of lattice dynamics was found to start about 15 ps after excitation.

Kurzzusammenfassung

Ultrakurze Laserpulse werden für die Bearbeitung einer Vielzahl von Materialien wie Metallen, Halbleitern und Isolatoren genutzt. Für die Entwicklung von Laserbearbeitungsverfahren ist es von entscheidender Bedeutung, den Einfluss von Laserparametern wie der räumlichen, zeitlichen und spektralen Pulsstruktur auf die Prozesse, die zum Materialabtrag führen, zu verstehen.
Um die während der Materialabtragung ablaufenden Prozesse zu entschlüsseln, wird in dieser Arbeit eine experimentelle Methode zur Beobachtung der Plasmadynamik in 30 nm dünnen Goldfolien, die mit einem intensiven 800 nm Femtosekunden (fs)-Anregepuls angeregt werden, vorgestellt. Die angeregte Folie wird mit einem fs-400 nm Abfragepuls geringer Intensität mit einer variablen Zeitverzögerung von bis zu 2 ns abgebildet und das Beugungsbild mit einem CMOS Detektor im Fernfeld aufgenommen. Die zeit- und ortsaufgelöste komplexe Transmission wird aus den aufgenommenen Beugungsbildern mit einem *phase retrieval* Algorithmus rekonstruiert. Ziel dieser Arbeit ist es, den Einfluss der Laserparameter, wie der Anregungsenergie und der Polarisation, auf die Plasmadynamik zu untersuchen. Eine Abnahme der Transmission mit steigender Pumpenergie in den ersten 10 ps wurde auf eine Zunahme der freien Elektronendichte zurückgeführt. Außerdem wurde festgestellt, dass die Gitterdynamik etwa 15 ps nach der Anregung einsetzt.

Contents

Chapter 1.

Introduction

Intense ultrashort laser pulses with pulse length in the pico- and femtosecond regime have been widely used in the past decades to machine a great variety of materials including insulators, semiconductors and metals [1, 2, 3]. With ultrashort pulses, high precision machining with a submicron resolution is achievable [4, 5, 6].
However, rather small changes in the pump pulse parameters can change the ablation dynamics drastically [5, 7]. Thus, knowledge of the influence of laser parameters such as the spatial, temporal and spectral pulse structure on the plasma dynamics is essential for tailored laser machining applications.
In this thesis, an experimental method for the imaging of the plasma dynamics in laser-excited, 30 nm thick gold foils is presented. The free-standing foils are excited by an intense focused femtosecond (fs) 800 nm pump pulse with adjustable pulse energy and polarization and the dynamics in the foil are imaged by a low intensity fs-400 nm probe pulse via *coherent diffraction imaging (CDI)*.
To resolve the processes in the excited foil, the complex transmission of the foil with a spatial resolution in the micrometer range and a temporal resolution in the fs regime is desirable. This is achieved by the lensless imaging technique CDI [8]. In CDI, a coherent probe beam is diffracted at the target and a diffraction image is captured with a detector placed in the far field. As the detector can only capture the intensity but not the phase of the diffracted electric field, the 2D spatially resolved complex transmission is reconstructed from the diffraction patterns using an iterative phase retrieval algorithm [9], giving access to the dynamics in the excited gold foil. The resolution of CDI is in principle only limited by the wavelength of the incident light [8]. As a consequence, the required resolution in the micrometer range can be achieved with the used 400 nm probe beam. By adjusting the time delay between the pump and probe pulses, time resolved imaging of the plasma dynamics is possible.

The gold foil is destroyed at the spot where the pump pulse excites it during each measurement, making it impossible to average multiple shots. As a result, the measurement must be conducted in single-shot geometry. Therefore, the reproducibility and reliability of the measurements are of great importance. Consequently, one goal of this thesis is to improve the beam stability and reproducibility of the experiment. With a stable setup in place, the influence of the pump beam polarisation and intensity on the plasma dynamics is investigated. A stronger decrease in transmission with increasing pump energy was observed in the first 10 ps and it was attributed to an increase in the free electron density due to the excitation of electrons by the pump pulse. It was also found that the onset of the lattice dynamics occurs with a time delay of about 15 ps.
The thesis is structured as follows: First, theoretical models describing the interaction of ultrashort laser pulses with metals are discussed. Thereafter, the experimental setup used for the imaging of plasma dynamics in thin gold foils is presented and the reproducibility of the measurements is evaluated. Afterwards, the recorded diffraction images are discussed and the influence of the energy and polarization of the pump pulse on the plasma dynamics is analyzed. Finally, reconstructions of the complex transmission at the target position are discussed to obtain knowledge of the plasma dynamics in laser excited thin gold foils.

Chapter 2.

Fundamentals of Light-Metal Interaction

In this thesis the excitation and relaxation dynamics in a thin gold foil excited by a $800\,\mathrm{nm}$ ultrashort laserpulse with a pulse duration of about $40\,\mathrm{fs}$ are investigated. This chapter focuses on the fundamental mechanisms involved in the interaction of light with metals. Those processes include the absorption of laser light by the electrons, the energy transfer from the electrons to the lattice, the following melting of the lattice and subsequently the ablation of material from the target.

2.1. Classical Description of Light-Metal Interaction

In this section the interaction of light with metals is described using a classical approach. The energy absorption of the $800\,\mathrm{nm}$ pulse by the electrons is discussed by employing the Drude model. For the subsequent transfer of energy from the electrons to the nuclei, a Two-Temperature model [10] is used that provides an estimate of the lattice melting time.

2.1.1. The Drude Model

The Drude Model is a classical approach to describe the response of electrons in a metal to an electric field. The model describes electrons in metals as freely moving particles in a periodic lattice of positively charged ions. Upon exposure to an electric field E, the force applied on the electrons is given by a driving force due to the acceleration of the electrons by the electric field and a dissipation term that resembles energy loss

due to collisions of electrons with the surrounding lattice.

$$m_e\ddot{x} = eE - \gamma m_e\dot{x} \tag{2.1}$$

Here m_e and e denote the electron mass and the elementary charge, respectively. The dampening term depends on the inverse collision time $\gamma = \frac{1}{\tau_c}$ times the electron velocity $\dot{x}$ and electron mass.
A detailed solution to this differential equation under the assumption of an alternating electric field like a laser field is discussed in my Bachelor thesis [11]. Here I only want to sketch the basic outcome as a basis for further discussions.
The material response of a metal in a laser field can be described by its dielectric function:

$$\varepsilon(\omega) = 1 - \frac{\omega_p^2}{\omega^2 + i\gamma\omega} \tag{2.2}$$

with the plasma frequency $\omega_p = \sqrt{\frac{e^2 n_e}{\varepsilon_0 m_e}}$ and ε_0 and n_e denoting the vacuum permittivity and the free electron density, respectively. Model parameters for gold are $\gamma = 0.107\,\mathrm{PHz}$ and $\omega_p = 13.23\,\mathrm{PHz}$ [12]. The complex refractive index is connected to the dielectric function through the relation:

$$\hat{n} = n + i\kappa = \sqrt{\varepsilon(\omega)} \tag{2.3}$$

The real part of the refractive index n leads to a shortening of the wavelength and, therefore, a reduction of the propagation speed in the medium, whereas the imaginary part κ leads to a damping of the electric field in the medium and, consequently, absorption.

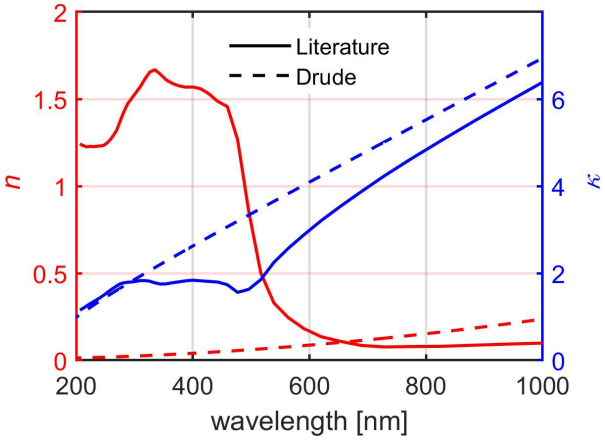

Figure 2.1.: Comparison of the real (n) and imaginary (κ) part of the refractive index of gold calculated by the Drude model (equations (2.2) and (2.3), dashed lines) and experimental values [13] (solid lines).

The Drude model can now be used to calculate the complex refractive index of gold in dependence of the wavelength. To discuss the accuracy of the model, the real and imaginary parts of the complex refractive index for gold as a function of the wavelength calculated with the Drude model, as well as the values obtained in [13] are shown in Fig. 2.1 for comparison. For wavelengths larger than $600\,\mathrm{nm}$, the Drude model is in good agreement with the data from [13]. However, when moving to shorter wavelengths the deviation from the literature values increases. This is due to relativistic effects that lead to absorption at rather low photon energies when compared to other metals [14].

The high average radial velocities of the inner s and p shells lead to a higher effective mass of the electrons and, therefore, a contraction of the average electron radius. However, the d and f electrons, due to their high angular momenta, are rarely near the nucleus and do not reach relativistic speeds. As a consequence, the relativistic effects for the outer orbitals are indirect. Due to the contraction of the inner orbitals, the nuclear attraction is screened more efficiently leading to a weaker attraction. The binding energy of the electrons with high angular momenta is decreased. As the binding energy is increased for s and decreased for d electrons, smaller energies are needed for interband absorption from the d to the s band. For gold this absorption sets in at around $540\,\mathrm{nm}$ [14] and leads to a refractive index evolution that can not be explained under the assumptions made by the Drude model. This explains the observed deviation of literature values to the Drude model for wavelengths smaller than $600\,\mathrm{nm}$. For other metals such as silver where relativistic effects are less significant, interband absorption is observed for smaller wavelengths in the UV-regime [14].

By using the refractive index obtained from the Drude model, the intensity absorbed by a metal foil with thickness L shall be calculated. Later we will use a $30\,\mathrm{nm}$ thick foil, which is smaller than the wavelength of the pump pulse of $\lambda = 800\,\mathrm{nm}$. This requires the consideration of multiple reflections at the boundaries of the foil and a coherent summation of the individual parts as illustrated in Fig. 2.2.

The expressions for the transmitted and reflected electric fields can be derived analytically and they boil down to (see attachment A.1):

$$E_T = \sum_i E_{Ti} = E_0 \cdot t_1 t_2 e^{\mathrm{i}kL} e^{-\alpha L} \frac{1}{1 - \left(r e^{-\alpha L} e^{\mathrm{i}kL}\right)^2} \tag{2.4}$$

$$E_R = \sum_i E_{Ri} = E_0 \left(r + t_1 t_2 r e^{-2\alpha L} e^{2\mathrm{i}kL} \frac{1}{1 - \left(r e^{-\alpha L} e^{\mathrm{i}kL}\right)^2} \right) \tag{2.5}$$

Here t_1 and t_2 denote the transmission coefficients for air to gold and gold to air, respectively. r is the reflectivity coefficient, α the absorption coefficient and $k = |\vec{k}|$ is the wave vector. They can be calculated with the following relations [15].

$$t_1 = \frac{2}{1+\hat{n}};\ t_2 = \frac{2\hat{n}}{1+\hat{n}};\ r = -\frac{1-\hat{n}}{1+\hat{n}};\ \alpha = \frac{2\pi\kappa}{\lambda};\ |\vec{k}| = \frac{2\pi n}{\lambda} \tag{2.6}$$

Since the intensity is proportional to the square of the electric field: $I \propto |E|^2$ and energy conservation has to be fulfilled, the absorbed intensity I_{abs} can be written in terms of laser intensity I_0:

$$|E_{\text{abs}}|^2 = |E_0|^2 - (|E_R|^2 + |E_T|^2) \tag{2.7}$$

$$I_{\text{abs}} = I_0 \cdot \left(1 - \frac{|E_R|^2 + |E_T|^2}{|E_0|^2}\right) \tag{2.8}$$

This allows for an estimation of the absorbed intensity and, therefore, of the deposited energy in the foil. Absorbed energy density values given throughout this thesis are calculated in this manner. The deposited energy in the foil is an important parameter

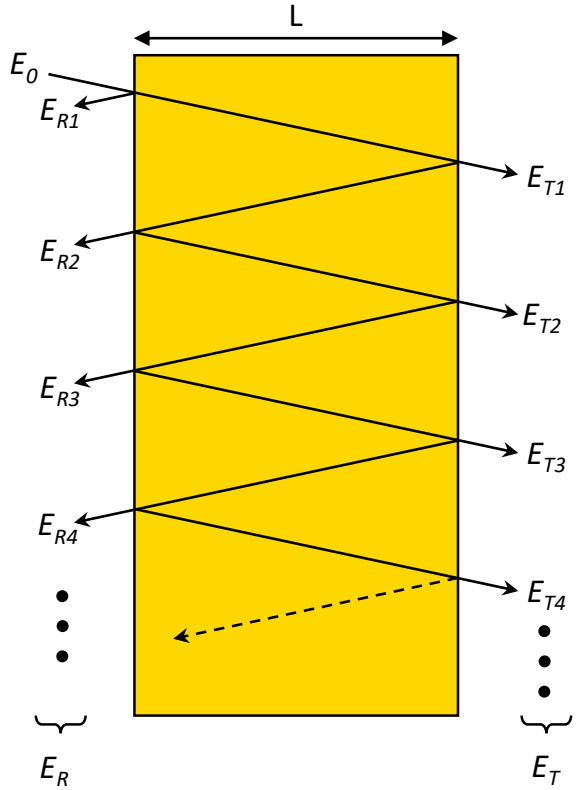

Figure 2.2.: Schematic diagram of the internal reflections inside a thin foil. E_0 represents the incoming electric field. E_R is the reflected electric field which is the sum of the contributions E_{Ri}, while E_T is the transmitted electric field and therefore the sum of the contributions E_{Ti}. For simplicity, only the first four contributions are shown. L denotes the thickness of the foil.

for simulating the dynamics after laser excitation. One way to quantify the energy transfer from the electrons to the nuclei and the melting of the material is the Two-Temperature Model.

2.1.2. The Two-Temperature Model

The absorption of a laser pulse hitting a metal target is mainly due to absorption by the electrons in the metal. This can be described by an increase in the electron temperature T_e following laser excitation. Due to electron-phonon coupling, the energy of the electrons is transferred to the lattice, resulting in an increase in the lattice temperature T_i. This energy exchange can be described by the Two-Temperature model (TTM) that was first introduced by Anisimov et al [10]. The energy exchange can be modeled by the equation[10, 3]:

$$c_i \frac{\partial T_i}{\partial t} = -c_e \frac{\partial T_e}{\partial t} = \zeta (T_e - T_i) \tag{2.9}$$

Here $c_i,$ and c_e denote the lattice and electron heat capacity, respectively, and ζ is the electron-phonon coupling constant. The rate of energy exchange is therefore proportional to the temperature difference between the electron and lattice systems.
However, as the temperature of the electrons follows the profile of the pump pulse, the foil temperature after excitation is highest in the center of the excited region and lowest in the surrounding material where the electrons are still at room temperature. This results in a temperature gradient in lateral direction. Furthermore, the electrons in the front of the foil will absorb more laser energy than the electrons in the back, as the laser intensity is higher at the front where no light has been absorbed yet. This leads to a second temperature gradient in laser propagation direction. The temperature gradients in lateral and laser propagation direction will result in heat conduction. Since an ideal Gaussian beam profile has radial symmetry, the transformation into cylindrical coordinates with r and z denoting the radial distance from the peak of the laser field and the axial coordinate in laser propagation direction, respectively, is natural. Including classical thermal conduction terms and taking into account the energy deposited by the laser pulse in the electronic subsystem Q, equation (2.9) is

extended to [3, 16]:

$$c_e \frac{\partial T_e}{\partial t} = \frac{1}{r}\frac{\partial}{\partial r}\left(\kappa_e r \frac{\partial T_e}{\partial r}\right) + \frac{\partial^2 T_e}{\partial z^2} - \zeta(T_e - T_i) + Q(r,z,t) \tag{2.10}$$

$$c_i \frac{\partial T_i}{\partial t} = \frac{1}{r}\frac{\partial}{\partial r}\left(\kappa_i r \frac{\partial T_i}{\partial r}\right) + \frac{\partial^2 T_i}{\partial z^2} + \zeta(T_e - T_i) \tag{2.11}$$

Here $\kappa_i,\ \kappa_e$ denote the thermal conductivity of the phonon and electron systems, respectively. As the conduction band electrons in metals have a high mobility, they can transfer heat efficiently through the material. As a consequence, heat conduction in metals is dominated by electrons [3, 17, 18]. As the contribution of the phonon system to the heat conduction is small compared to the contribution by the electrons, the phonon heat conduction is neglected.
Additionally, ballistic electron transport is observed when the mean free path of the electrons is larger than the characteristic length of the target. The ballistic range in gold is estimated to exceed $100\,\mathrm{nm}$ [19, 20] and is, therefore, larger than the thickness of the gold foils studied in this thesis ($30\,\mathrm{nm}$). Since ballistic electron transport leads to a highly efficient distribution of the laser energy, it is save to assume that the foil is homogeneous heated throughout its entire thickness. Nonetheless, heat conduction in the lateral direction still has to be taken into account. This leads to the following equations:

$$c_e \frac{\partial T_e}{\partial t} = \frac{1}{r}\frac{\partial}{\partial r}\left(\kappa_e r \frac{\partial T_e}{\partial r}\right) - \zeta(T_e - T_i) + Q(r,t) \tag{2.12}$$

$$c_i \frac{\partial T_i}{\partial t} = \zeta(T_e - T_i) \tag{2.13}$$

Lastly, as gold is melted, the latent heat of fusion must be considered. This is achieved by restricting the increase in lattice temperature beyond the melting point until the necessary latent heat of fusion is transferred from the electron system to the lattice.
With this model we can now predict the temperature evolution in the gold foil. The temperature ahead of irradiation is room temperature, i.e. $T_e = T_i = 293\,\mathrm{K}$. The parameters for the electrons and lattice in gold are: the heat capacity of the electronic system $c_e = \sigma T_e$ with the proportionality factor $\sigma = 0.725\,\mathrm{mJ\,mol^{-1}\,K^{-1}}$ [19], the heat capacity of a gold ion lattice $c_i = 25.122\,\mathrm{J\,mol^{-1}\,K^{-1}}$ [21] and the electron phonon coupling constant $\zeta = 2.04 \times 10^{11}\,\mathrm{W\,mol^{-1}\,K^{-1}}$ [19]. The latent heat of fusion for gold is $H_{\mathrm{fus}} = 12.6\,\mathrm{kJ\,mol^{-1}}$ [22] and the melting temperature is $T_{\mathrm{melt}} = 1337.33\,\mathrm{K}$ [23].

The Gaussian laser pulse has a pulse duration of $50\,\mathrm{fs}$ (FWHM), a beam radius of $15\,\mu\mathrm{m}$ and a pulse energy of $3.7\,\mu\mathrm{J}$. The absorbed pulse energy was calculated using equation 2.8 and is $0.11\,\mu\mathrm{J}$. This results in deposited energy density in the center of the beam of $0.54\,\mathrm{MJ\,kg^{-1}}$.

In Fig. 2.3, the numeric solution to the TTM equations (2.12, 2.13), with the latent heat of melting included as discussed above, is presented. In the initial few picoseconds (ps) following irradiation, the lattice temperature (right image) remains close to room temperature, while the electron temperature (left image) experiences a rapid ascent to roughly $14\,000\,\mathrm{K}$. Due to the electron-phonon coupling, the energy of the electrons is now transferred to the lattice. After $10\,\mathrm{ps}$, the lattice heats up and reaches a temperature that approaches the melting temperature of gold, denoted by the dashed

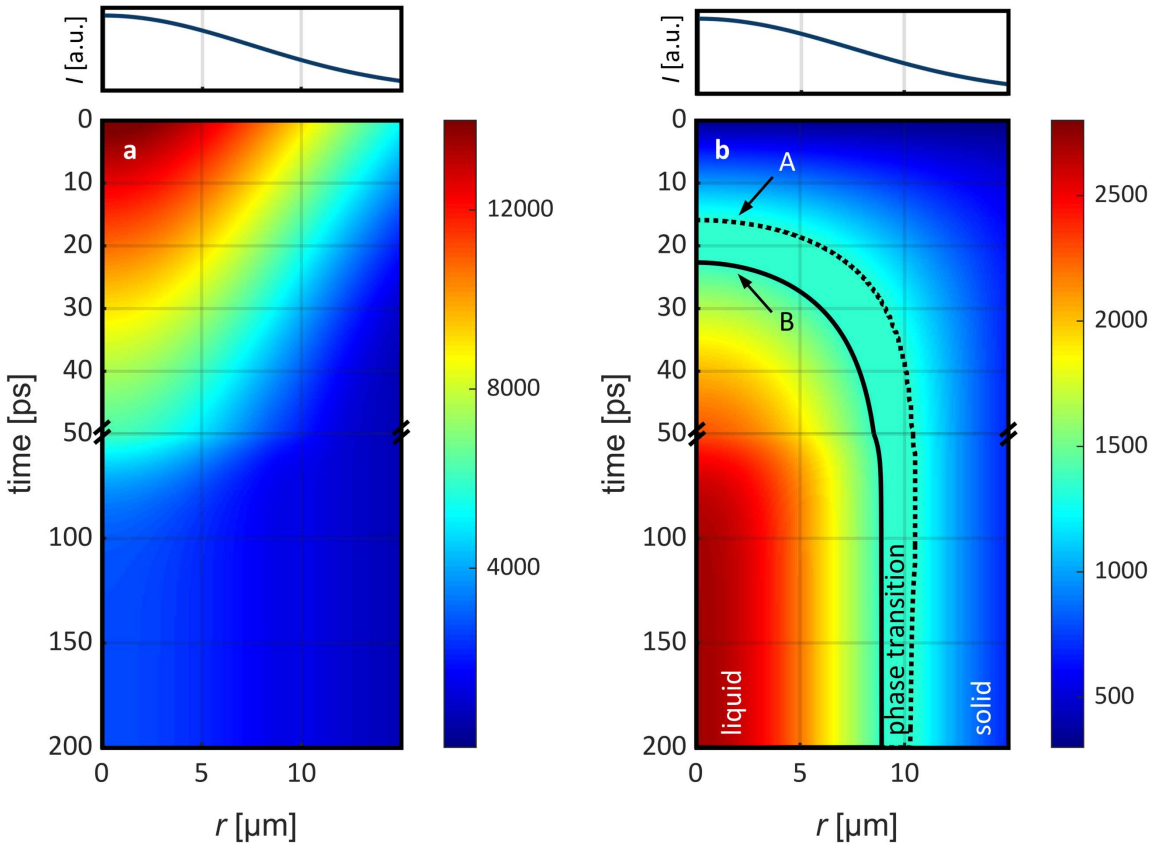

Figure 2.3.: Temporal and spatial evolution of the a) electron and b) lattice temperature according to the TTM (eq. (2.12,2.13)) for a $30\,\mathrm{nm}$ thick gold foil irradiated by a Gaussian laser pulse with a pulse length of $50\,\mathrm{fs}$ (FWHM), a beam radius of $15\,\mu\mathrm{m}$ and a pulse energy of $3.7\,\mu\mathrm{J}$. The lateral intensity profile of the laser pulse in arbitrary units is shown on top of the figures with the same $x-$axis. The dotted and solid lines represent the onset of melting and finished melting, respectively. The absorbed pulse energy is calculated according to equation (2.8). The parameters describing the foil are discussed in the text.

line. Approximately $15\,\mathrm{ps}$ after irradiation, the lattice temperature reaches the melting point in the center of the beam, indicated by the dashed line (see arrow A). $20\,\mathrm{ps}$ after irradiation a region with a radius of more than $5\,\mu\mathrm{m}$ undergoes the melting process. During this phase, any further energy input into the lattice system is absorbed by the melting process, specifically through the latent heat of fusion. Only $25\,\mathrm{ps}$ after irradiation, the melting is completed in the center of the beam (see arrow B). After $60\,\mathrm{ps}$, all material within a $8\,\mu\mathrm{m}$ radius is completely molten and from $8\,\mu\mathrm{m}$ to $11\,\mu\mathrm{m}$ the gold is partially molten.

For times larger than $60\,\mathrm{ps}$, there are no mayor changes in the size of the melted region. However, the temperature of the lattice in the center of the beam increases until $100\,\mathrm{ps}$ after irradiation and reaches a maximum temperature of $3500\,\mathrm{K}$. From there on, the temperature of the lattice and electrons stays nearly constant. Note, that the temperature profile closely mirrors the intensity profile of the laser pulse, except for the region of constant temperature about $10\,\mu\mathrm{m}$ from the center, where the lattice is only partially melted. Now the only mechanism changing the temperature profile is heat conduction. However, this process does not seem to play a major role on the studied length and time scales in the range of micrometers and picoseconds as the temperature profile of the electron and lattice system does not change significantly anymore.

The TTM allows for a prediction of the behavior of metals from the excitation by a laser pulse until melting. One can estimate intensity thresholds for melting and even ablation, if an ablation temperature can be defined [24], and extract timescales for electron-lattice relaxation. However, the model has its limits. The timescales predicted by the TTM are significantly influenced by material parameters, particularly the electron-phonon coupling parameter ζ, whose values show notable variations in the existing literature from $2 \times 10^{11}\,\mathrm{W\,mol^{-1}\,K}$ to $3 \times 10^{11}\,\mathrm{W\,mol^{-1}\,K}$ [19, 25, 26, 27, 28]. Furthermore, the studied systems are strongly excited, which may lead to changes of the material parameters as the electron and phonon systems are relaxing. For example, in [29] it has been proposed, that the electron phonon coupling depends on the temperature of the electrons as well as the phonon system.

In summary, the TTM allows for a prediction of the characteristic timescales of lattice heating and melting. However, the model has some limits and, therefore, the results should be approached with caution and considered as guidelines rather than definitive predictions.

2.2. Laser Melting and Ablation

In this section, more sophisticated models and experimental studies used to describe the interaction of light with metals are discussed. The studies are sorted into two different laser fluence regimes in order of increasing fluence: 1) heterogeneous melting and 2) homogeneous melting regime. The results of the studies are compared to predictions acquired with the TTM in section 2.1.2.

2.2.1. Heterogeneous Melting

For absorbed energy densities ranging from approximately $0.1\,\mathrm{MJ\,kg^{-1}}$ to $0.4\,\mathrm{MJ\,kg^{-1}}$ and for laser pulses shorter than $200\,\mathrm{fs}$, the dominant melting process is heterogeneous melting [30, 31]. It is not expected that this melting mechanism is the dominant mechanism for measurements in this thesis, as the energy densities studied in this work range from $0.5\,\mathrm{MJ\,kg^{-1}}$ to about $7\,\mathrm{MJ\,kg^{-1}}$. Nevertheless, the process of heterogeneous melting is discussed in this section, since it could be observed at some distance from the center of the excited region, as the intensity of the pump pulse will be reduced there.
Heterogeneous melting is characterized by distinct melting fronts that originate from surfaces or crystal defects and then propagate through the metal. Propagation speeds of the melting front of several hundreds $\mathrm{m\,s^{-1}}$ have been observed experimentally [32, 33]. For the thin $30\,\mathrm{nm}$ gold film used in this thesis, heterogeneous melting would lead to an expected melting time of about 100 picoseconds. This estimation of the melting time is consistent with theoretical studies, where a combination of the TTM and molecular dynamics simulations were used [30, 34], as well as experimental studies [31] investigating the melting of thin gold foils. Thin film melting is accompanied by oscillating pressure waves in the film and the amplitude of those waves depends strongly on the rate of energy transfer between the electron and lattice system [30]. For strong electron phonon coupling e.g., in nickel and sub picosecond laser pulses, the lattice does not have the opportunity to expand, leading to high pressure waves in the foil. For gold films, the energy exchange between electrons and lattice is slow, and the material can expand during the heating of the lattice, resulting in weaker pressure waves when compared to other metals [30]. It was proposed that heterogeneous melting only occurs below the ablation threshold for thin films [30]. Nonetheless, the phase change from solid to liquid may lead to a change in the refrac-

tive index and, as a consequence, should be observable in the experiment, even if no material ablation is present.
The simple TTM discussed in section 2.1.2 suggests a melting time for complete melting of 45 picoseconds for a peak energy density of $0.38\,\mathrm{MJ\,kg^{-1}}$ (result not shown). As discussed above, other theoretical studies suggest a melting time of $100\,\mathrm{ps}$ [30, 34] for a similar energy density. While the melting time estimated by the simple TTM roughly aligns with studies in terms of order of magnitude, it consistently underestimates the actual melting time. This is most likely due to an oversimplified description of the melting process in the simple TTM. The only parameter deciding the melting of the foil in the simple model is the energy deposited in the lattice system. It is assumed that the lattice melts instantaneously if enough energy is deposited in the lattice. However, the melting process further depends on effects like a change in the melting temperature due to pressure waves in the foil. In addition, the melting only starts at crystal defects and surfaces. These effects can prolong the melting time, even though the energy required for melting is already transferred to the lattice, leading to a longer melting time when compared to the simple TTM.

2.2.2. Homogeneous Melting

At higher absorbed energy densities in the range of $0.4\,\mathrm{MJ\,kg^{-1}}$ to $1.0\,\mathrm{MJ\,kg^{-1}}$, the dominant melting process changes to homogeneous melting [30, 31, 34]. In contrast to heterogeneous melting, homogeneous melting lacks clear melting fronts. Instead, the film melts due to homogeneous nucleation throughout the entire film. This results in reduced melting times in the range of $10\,\mathrm{ps}$ to $50\,\mathrm{ps}$ [30, 31, 34]. This is in good agreement with the simple TTM, which suggests a melting time in the center of the beam of $25\,\mathrm{ps}$ for a peak energy density of $0.54\,\mathrm{MJ\,kg^{-1}}$, as can be seen in Fig. 2.3. The results of the simple TTM can therefore serve as a rough estimate for the timescales of laser-induced melting of thin foils.
For the disintegration of a gold film with a thickness of several tens of nanometers, as used in this thesis, an absorbed energy density of $1.0\,\mathrm{MJ\,kg^{-1}}$ or more is necessary which leads to the final film temperature exceeding the boiling temperature of gold [30]. The disintegration of the film involves the heating of the lattice and subsequent homogeneous melting after some picoseconds, as described above. The heating and melting of the lattice results in a buildup of compressive pressure, which drives the expansion of the gold film along the surface normal starting roughly at $10\,\mathrm{ps}$. This expansion leads to the splitting of the foil in the middle after roughly $60\,\mathrm{ps}$. The

disintegration of the gold film is accompanied by the boiling of the gold and, therefore, the release of gas-phase gold atoms [30]. The two liquid regions will now expand outward, i.e. along the surface normal. For a Gaussian laser intensity profile, one expects a plume formation. This is due to the higher excitation energy in the center of the beam, which causes the liquid fronts to move faster in the center than at the outer edge of the laser spot [35].

It should be noted, that in addition to the ablation due to an increased lattice temperature, also a Coulomb explosion could lead to ablation of the gold foil. A Coulomb explosion occurs when a target is rapidly ionized, for example by an intense, ultrashort laser pulse [36]. The remaining positively charged ions now repulse each other which may lead to a disintegration of the foil. However, Coulomb explosion effects only seem to be important close to the ablation threshold, i.e. for ablation depths of less than $20\,\mathrm{nm}$ [37]. Most of the measurements in this thesis where conducted at higher intensities where thermal ablation is the dominant effect.

However, detailed descriptions of the mechanisms behind the ablation of the metal foil due to thermal expansion are hard to come by. Most of the theoretical studies in the energy regimes discussed above are using a model combining the TTM with molecular dynamics (MD) simulations [3, 30, 34]. The TTM is used to describe the laser energy absorption by the electrons, the energy transfer from the electrons to the lattice and the heat conduction by the electrons, whereas the MD simulation is used to simulate the nuclei and, therefore, processes of lattice melting and disintegration of the material. In MD simulations, the force acting on a particle is evaluated by using interatomic potentials and the trajectory of the particle is changed accordingly for each time step. The computational effort needed for such a simulation increases strongly with the number of particles that are simulated. To mimic the response of larger systems, periodic boundary conditions are applied and a constant laser energy deposition is assumed over the whole simulation area.

However, if one wants to study how targets responds across the entire laser spot, considering variations in energy deposition in lateral direction, MD simulations are not suitable. This is because simulating all atoms in the gold foil for the entire laser spot, which is several micrometers in size, requires too much computational effort, since the number of particles in the system is too large.

Attempts to predict the behavior of a target exposed to a non-constant laser fluence due to the lateral profile of a laser beam have been made by employing a so called mosaic approach. In the mosaic approach, results from individual TTM-MD simulations that were taken at the same time are combined according to their local fluence in

the laser spot, to represent the laser induced processes at the scale of the whole laser spot [38]. However, this method cannot resolve effects that occur due to pressure and temperature gradients in lateral direction.
Another method to calculate the response of metals to laser fields are so called particle-in-cell (PIC) simulations [39]. In those simulations, individual particles are tracked in a continuous space whereas charge densities and currents are computed simultaneously on a grid. The forces acting on the particles are then calculated by interpolating the fields from the grid points to the particles in the continuous phase space. This method was designed for weakly coupled systems which is the case for hot and diffuse plasmas. In this case, the particles in the plasma can be treated as if they are only interacting with a background field rather than taking individual collisions into account. Therefore, PIC simulations are applicable for studies where ultrahigh intensities allow for the assumption of fully ionized targets and hot plasmas. In those regimes, effects like the piston push effect [40], the formation of plasma jets [41] or electron jets [42] have been observed. However, since those intensities exceed the intensities studied in this thesis, those effects will not be discussed further.
In summary heterogeneous melting of the gold film is expected for absorbed energy densities in the range of $0.1\,\mathrm{MJ\,kg^{-1}}$ to $0.4\,\mathrm{MJ\,kg^{-1}}$ with a melting time in the vicinity of $100\,\mathrm{ps}$. When the energy density is increased to a range of $0.4\,\mathrm{MJ\,kg^{-1}}$ to $1.0\,\mathrm{MJ\,kg^{-1}}$, the melting type is expected to convert to homogeneous melting. Expected melting times are reduced to $10\,\mathrm{ps}$ to $50\,\mathrm{ps}$. Disintegration of the material is only expected for an energy density of more than $1.0\,\mathrm{MJ\,kg^{-1}}$. Then, after the homogeneous melting, the disintegration of the foil is expected after a time of roughly $60\,\mathrm{ps}$. Furthermore, the simple TTM introduced in section 2.1.2 can be used to estimate the melting time of the gold foil for different energy densities.

Chapter 3.

Experimental Setup and Methods for Plasma-Analysis

The goal of this thesis is to study the plasma dynamics in a laser excited thin gold foil using a single-shot pump-probe imaging setup. The target, a $30\,\mathrm{nm}$ thick gold foil, is excited by an intense $800\,\mathrm{nm}$ pump pulse with a pulse duration in the femtosecond regime. After an time delay adjustable up to $2\,\mathrm{ns}$, the dynamics are imaged by a $400\,\mathrm{nm}$ probe pulse with a similar pulse duration. The probe pulse should not influence the excitation and relaxation dynamics in the foil. Therefore, the probe intensity is chosen low compared to the pump pulse. After the target is excited by the pump pulse, the probe pulse is diffracted at the target and a diffraction image is captured by the detector. The diffraction image is used to obtain information about the plasma dynamics in the excited gold foil by analyzing the structure and total intensity of the images. Furthermore, the complex electric field including amplitude and phase at the target position is reconstructed from the diffraction images using a phase retrieval algorithm that was developed by R. Altenkirch and C. Peltz at the Institute of Physics, University of Rostock in the group of Prof. Fennel.
In this chapter, the experimental setup and the measurement procedure for the imaging of the plasma dynamics in thin gold foils is explained. Afterwards, the stability of the setup and the reproducibility of the measurements is discussed. Finally, a method to measure the spatially resolved thickness of the gold foil is presented.

3.1. Experimental Setup for Imaging Plasma Dynamics in Thin Gold Foils

The setup for imaging the plasma dynamics is shown in Fig. 3.1. A Ti:Sa laser (Spitfire Ace PA, Newport) with a center-wavelength of $800\,\mathrm{nm}$ and a pulse length of $40\,\mathrm{fs}$ is used. While the laser typically operates at a repetition rate of $1\,\mathrm{kHz}$, the repetition rate is reduced to $50\,\mathrm{Hz}$ for single-shot measurements. The low repetition rate is necessary for the selection of single probe pulses for the imaging, as well as the selection of single pump pulses for the excitation, since the temporal spacing between two pulses has to be larger than the camera's integration time, which is $20\,\mathrm{ms}$ and shutter's closing time of $7\,\mathrm{ms}$.

For the experiment, an intense pump pulse that induces material modifications as well as a low intensity probe pulse for the imaging of the excitation and relaxation dynamics in the foil are required. In addition, an adjustable time delay between the pump and probe pulses is necessary to obtain time-resolved measurements.

To meet the these requirements, the primary beam is divided using a beam splitter. The reflected beam, containing $10\,\%$ of the primary beam's pulse energy of about $1\,\mathrm{mJ}$, serves as the probe beam, whereas the transmitted beam is used as the pump beam.

As the probe beam is used to image the plasma dynamics in the foil and a high spatial resolution is desirable, a shorter wavelength is needed for the probe beam. Addi-

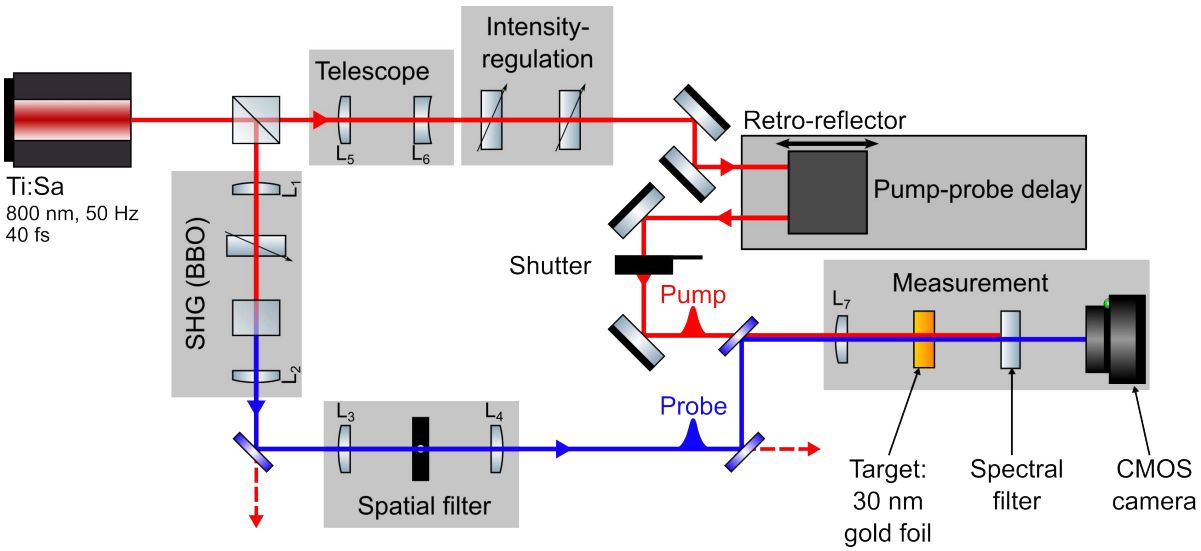

Figure 3.1.: Experimental setup for the imaging of plasma dynamics in thin gold foils. The red lines indicate the 800 nm fundamental and the blue line the 400 nm of the second harmonic. Apertures are not shown in the sketch.

tionally, altering the probe beam's wavelength makes it possible to separate it from the pump beam before the camera with a spectral filter. The method of choice to reduce the laser wavelength is second harmonic generation (SHG) by using a barium borate crystal (BBO). This decreases the wavelength of the probe pulse from $800\,\mathrm{nm}$ to $400\,\mathrm{nm}$. The BBO is placed in the focal point of lens L_1 ($f = 500\,\mathrm{mm}$) and lens L_2 ($f = 200\,\mathrm{mm}$). To remove the remaining $800\,\mathrm{nm}$ component from the probe beam, dielectric mirrors with a high reflectivity at $400\,\mathrm{nm}$ and low reflectivity at $800\,\mathrm{nm}$ are used.
The diffraction image of the probe beam is captured by a CMOS camera (Neo 5.5 sCMOS, Andor). To extract as much information as possible from the measurement, it is crucial to capture the maximum amount of diffraction orders whilst not oversaturating the camera sensor with the primary beam. Therefore, an intensity regulation consisting of two polarization sensitive optics, a polarizing filter and the BBO, is used. As only the horizontal component of the incoming light is frequency doubled by the BBO due to the phase matching condition, the intensity of the probe beam can be adjusted steplessly by rotating the polarizing filter. Hence, the probe beam intensity is set to use the entire dynamic range of the detector.
As the probe beam is used for coherent diffractive imaging of the plasma dynamics, it is crucial that the beam has a Gaussian beam profile. However, the beam profile is worsened by the SHG stage. To reach a high-quality beam profile, a spatial filter consisting of two lenses, L_3 ($f = 300\,\mathrm{mm}$) and L_4 ($f = 100\,\mathrm{mm}$) and a pinhole with a diameter of $100\,\mu\mathrm{m}$ in the focal point of both lenses is used. In addition, the focal length of the two lenses are chosen such, that the beam diameter shrinks to below $2\,\mathrm{mm}$. This small beam diameter is required to achieve an optimal relative size between pump and probe focus on the target. The size requirements of pump and probe beam are discussed in section 3.2. Further refinement of the beam profile is achieved through the use of apertures, which are utilized to eliminate unwanted diffraction rings produced by the pinhole. This ensures an optimal beam quality for imaging purposes.
The following section will address the beam path of the pump beam. To be able to guide the pump beam through optics like the retro reflector, the beam diameter of $12\,\mathrm{mm}$ from the laser output has to be reduced to a smaller diameter that is reasonable for the used optics. Therefore, a telescope consisting of two lenses, L_5 ($f = 500\,\mathrm{mm}$) and L_6 ($f = -300\,\mathrm{mm}$), positioned $200\,\mathrm{mm}$ apart, is used, which reduces the beam diameter from $12\,\mathrm{mm}$ to about $7\,\mathrm{mm}$. As time resolved measurements of the plasma dynamics are the goal of this thesis, a method to delay the probe relative to the pump pulse is needed. The delay between pump and probe pulse is accomplished by a linear

stage with $30\,\mathrm{cm}$ travel, resulting in a maximum time delay of roughly $2\,\mathrm{ns}$. Furthermore, as the dependence of the plasma dynamics on the pump intensity and polarization are of interest, two polarizers are used to adjust both parameters continuously by either turning the first or the second polarizer.
For imaging the plasma dynamics, the pump and probe pulse have to reach the target co-linear as they will be focused by the same lens. The spatial overlap is reached by joining both beams using a dielectric mirror that reflects the $400\,\mathrm{nm}$ light and is transparent for the $800\,\mathrm{nm}$ light. Both co-linear beams are then focused by lens L_7 ($f = 50\,\mathrm{mm}$) onto the target, a $30\,\mathrm{nm}$ thick gold foil. As only the probe beam shall be recorded by the camera, the pump beam is filtered out by a bandpass filter (FB400-40, Thorlabs) that is only transparent for the probe light. To extract as much information as possible from the diffracted probe beam, the distance of the camera from the target is chosen such that the entire detector area is covered with the diffraction image without cutting off any diffraction orders.
A major issue in previous measurements prior to this thesis was the correct timing for triggering the camera and shutter. The shutter was manually opened for $20\,\mathrm{ms}$ (the time between two pulses at a repetition rate of $50\,\mathrm{Hz}$), and the camera was triggered by the shutter's trigger output. This often resulted in unusable measurements, as the shutter sometimes allowed two pump pulses to pass, or the camera detected two probe pulses simultaneously. This problem was successfully solved by using a microcontroller (Arduino-Nano) connected to the laser trigger output for the triggering. This synchronizes the triggering of both the camera and the shutter with the laser. With this system in place, always one pump pulse is selected for excitation, and one probe pulse is captured for imaging.

3.2. The Geometry of the Diffraction Setup

In this section, a detailed explanation of the interaction zone, i.e. the region where the pump pulse excites the gold foil and the dynamics are imaged by the probe pulse, is given. To successful image the dynamics, the geometry of the diffraction setup, including the interaction zone, is crucial. The diffraction setup is shown in Fig. 3.2.
To avoid imaging errors, an aspheric lens (Sill Optics) is used to focus the pump and probe pulse onto the thin gold foil. The pump beam, which has a beam radius in the focus of about $15\,\mu\mathrm{m}$, excites a region in the gold foil. Then, the probe beam is diffracted at this interaction zone and the detector, placed about $10\,\mathrm{cm}$ behind the target, captures a diffraction image of the probe beam. This image consists of two parts:

One part of the probe beam is transmitted through the foil outside of the interaction zone, where the foil is still undisturbed. The other contribution stems from the part of the probe beam that illuminates the excited region. It is diffracted at the interaction zone. Both contributions are superimposed on the detector. For successful imaging of the dynamics in the foil, the relative intensity and relative size of the transmitted and scattered contribution on the detector is crucial.
The relative intensity of both contributions can be controlled by adjusting the size of the excited region relative to the probe beam size at the target position. A small probe beam increases the contribution of the diffracted light and a large probe beam increases the contribution of the light transmitted through the foil. To adjust the relative size of the contributions on the detector, the position of the foil along the propagation direction is varied. If the foil is placed closer towards the detector, the area on the detector that is illuminated by diffracted light is smaller. The ideal experimental parameters for the current setup are discussed later on in this section.
To get insights into the plasma dynamics in the foil, the complex electric field, including amplitude and phase, at the target position shall be obtained. The calculation of the complex electric field at the target position requires that the electric field at the detector position is known. However, the detector can only capture the intensity, which means that the phase information of the field is lost.
To obtain the electric field at the target position from the diffraction image, iterative phase retrieval [9] is used. The algorithm to used in this thesis to reconstruct the electric field was developed by R. Altenkirch and C. Peltz and a detailed explaination

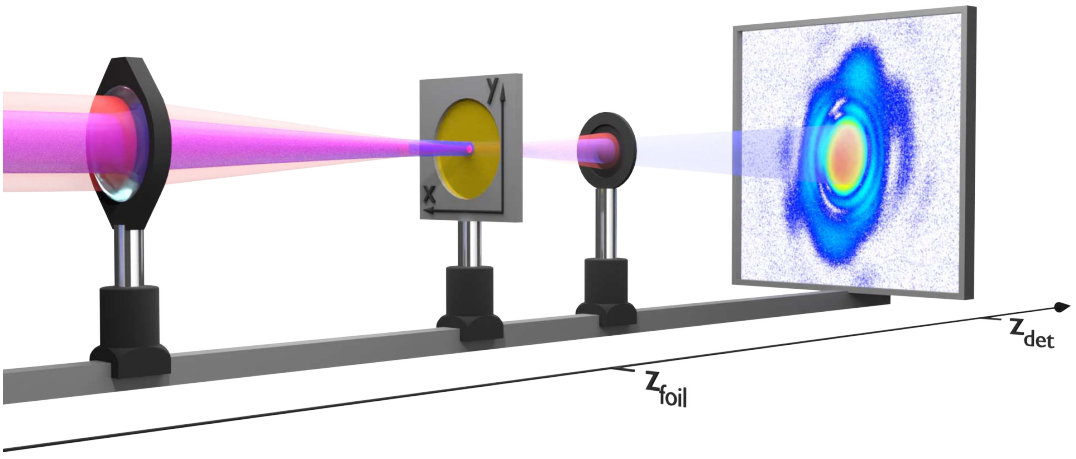

Figure 3.2.: The setup for coherent diffractive imaging of the plasma dynamics. Lens L_7 focuses the pump (red) and probe (blue) pulse onto the gold foil. The pump pulse is filtered out by the bandpass filter behind the target and a diffraction image of the probe pulse is captured with the detector.

is given in the master's thesis of R. Alternkirch [43]. One crucial step in the phase retrieval procedure is the numerical propagation of an arbitrary electric field from the detector plane to the target plane and vice versa.
One method for numerical propagation of a given electric field is the angular spectrum method [44]. If a given electric field at the target position $E(x', y', 0)$ is known, the electric field at the detector position $E(x, y, z)$ can be calculated by:

$$E(x', y', z) = \mathcal{F}^{-1}\left[\mathcal{F}[E(x, y, 0)]e^{ikz\sqrt{1-\alpha_x^2-\alpha_y^2}}\right] \tag{3.1}$$

with $\alpha_i = k_i c$ being the wave vectors x and y components multiplied by the speed of light c and $\mathcal{F}$ and $\mathcal{F}^{-1}$ resembling Fourier- and inverse Fouriertransformations. However, this method is not suitable for fields that diverge in x-y direction.
To resolve the target with high accuracy, a high spatial resolution and as a consequence, a small grid size is desireable in the focus. As the beam diverges with increasing distance from the target, a large area at the detector plane is needed to capture the whole image. However, in ASM the same grid size and resolution has to be used in both the target and detector plane. For strong diverging fields, as it is the case in the presented setup, many grid points are needed for to achieve sufficient resolution at the target position, whilst capturing the total diffraction image. This ultimately leads to a high computational effort, such that this method is not suitable for the here considered experimental geometry.
One computationally feasible approach is the numeric propagation of electric fields using the Fraunhofer diffraction equation [44]:

$$E(x, y, z) \approx \frac{ze^{ik\rho}}{i\lambda\rho^2} \iint_{-\infty}^{\infty} E(x', y')e^{-i\frac{k}{z}(x'x+y'y)}\mathrm{d}x'\mathrm{d}y' \tag{3.2}$$

A sketch illustrating the diffraction geometry and coordinate system used is shown in Fig. 3.3.
The advantage of this propagation method is, that the simulation area for the target and detector plane can have different sizes. Therefore, this method is computationally cheap even for strongly divergent fields.
However, the derivation of the Fraunhofer diffraction equation involves strong approximations, which make the formula only valid, if the Fraunhofer condition is fulfilled. The Fraunhofer condition reads [44]:

$$z \gg \frac{\pi}{\lambda}(x'^2 + y'^2)_{\max} \tag{3.3}$$

This conditions states, that the propagation distance z must be much larger than the size of the target divided by the wavelength. The parameters in the used setup, with $r'_{\text{max}} = \sqrt{x'^2 + y'^2}_{\text{max}}$ being the radius of the holes, are: $\lambda = 400\,\text{nm}$ and $r'_{\text{max}} \approx 25\,\mu\text{m}$. This leads to the following condition for the propagation distance:

$$z \gg 0.5\,\text{cm}$$

The distance between target an detector in the experiment is about $10\,\text{cm}$. Therefore, the condition is fullfilled. However, this methods fails quickly, if the size of the target increases, as the minimal required propagation distance scales quadratic with the target size.

To allow an accurate propagation of the electric field even for larger targets, a new diffraction formula, which in essence is a combination of the Fraunhofer and the Fresnel (see [44]) diffraction equation, was developed by R. Altenkirch and C. Peltz. It reads [43]:

$$E(x,y,z) \approx \frac{kze^{ik\rho}}{2\pi i\rho^2} \iint_{-\infty}^{\infty} E(x',y') e^{i\frac{k}{2z}(x'^2+y'^2)} e^{-i\frac{k}{z}(x'x+y'y)} \mathrm{d}x'\mathrm{d}y' \tag{3.4}$$

With the condition:

$$z^3 \gg \frac{|(r-r')^4 - r^4|_{\text{max}}}{4\lambda} \tag{3.5}$$

Here, $(r-r')$ is the difference in size of the diffracting target and the diffraction pattern in x-y-direction.

The propagation method is similar to the Fraunhofer propagation technique, but includes an additional phase term under the integral. This phase term stems from the Fresnel approximation, where the propagating spherical wavefronts are approximated

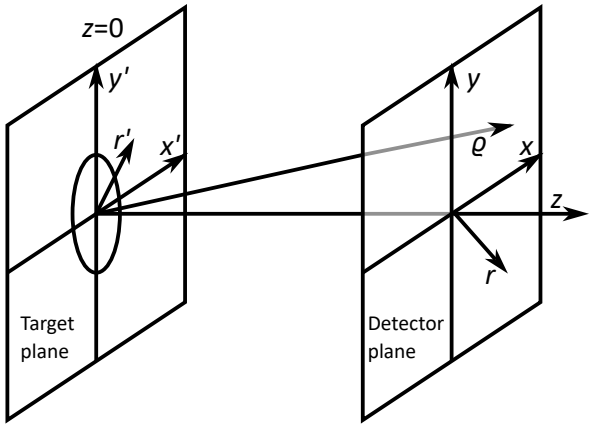

Figure 3.3.: Sketch showing the diffraction geometry and coordinate system. The incoming probe beam is diffracted in the target plane and the diffraction image is captured in the detector plane.

by parabolic wavefronts. This leads to a more accurate propagation for larger targets in the target plane.
For the above parameters and a maximal detector width of $2\,\mathrm{cm}$ this leads to following condition for the hybrid approximation:

$$z \gg 4.0\,\mathrm{cm}$$

On first glance, this condition is more restricting than the Fraunhofer condition. However, the scaling of the minimal propagation distance is not quadratic anymore and the method is applicable for target sizes of even $300\,\mu\mathrm{m}$, where the minimal propagation distance is about $9\,\mathrm{cm}$. In comparison, the required propagation distance in the Fraunhofer approximation for an target size of $300\,\mu\mathrm{m}$ is already about $18\,\mathrm{cm}$.
Since the hybrid approximation allows the accurate propagation of electric fields from the target to the detector and vise versa for the presented setup, it is used in the phase retrieval algorithm developed by R. Altenkirch and C. Peltz.
Apart from the ideal propagation method, other factors to consider for successful electric field reconstruction are the relative size and intensity of the scattered and transmitted probe pulses on the detector, as discussed at the beginning of this section. The relative size of the scattered and transmitted light can be adjusted by varying the distance of the gold foil to the detector and the relative intensity can be adjusted by varying the size of probe beam with respect to the size of the excited region in the foil. Theoretical studies by R. Altenkirch have shown that for a successful reconstruction of static holes in the foil, two main conditions must be met: 1) the object diameter, i.e. diameter of the holes after the excitation by the pump beam, should be roughly the same size as the probe beam radius at the target position $w(z_{\text{foil}})$ and 2) the gold foil and, therefore, the point of diffraction of the probe beam z_{foil}, should be some millimeters in front of the probe beam focus z_0. To fulfill these conditions, it's crucial that the beam waist of the pump beam is smaller than that of the probe beam.
The beam waist radius w_0 of a Gaussian beam is given by:

$$w_0 = \frac{2\lambda f}{\pi w_L} \tag{3.6}$$

Here, λ represents the wavelength, f is the focal length of the focusing lens, and w_L denotes the beam radius before the lens. Since both beams pass the same lens, and the wavelength of the probe beam ($\lambda = 400\,\mathrm{nm}$) is smaller than that of the pump beam ($\lambda = 800\,\mathrm{nm}$), the beam waist of the probe beam will be smaller, if the beam radius

prior to the lens is equal for the pump and probe beam. To still achieve a smaller beam waist for the pump beam, a larger pump beam radius prior to the lens compared to the probe beam is required. This is achieved by reducing the beam size of the probe beam in the SHG stage as well as in the spatial filter by using a lens with long focal length for focusing and a lens with shorter focal length for recollimation. Furthermore, the pump beam is kept as large as possible. However, an upper limit of the pump beam diameter is given by the used optics such as the retroreflector or shutter. A pump beam that does not fit the size of the optics would lead to a cutoff of part of the beam, causing artifacts in the beam profile. As a consequence, the focal length of the lenses in the telescope are chosen in a way that the pump beam is as large as possible whilst having an appropriate size for the used optics. This ultimately leads to a smaller focus size for the pump beam when compared to the probe beam, even though the wavelength of the pump beam is larger.

Another crucial factor for a successful reconstruction of the electric field is the knowledge of the geometry of the diffraction setup and interaction region. This includes the $z-$position of the target, the $z-$position of the detector and the beam parameters of the probe beam.

As the target, a $30\,\mathrm{nm}$ gold foil, is placed in a positioning system (HCU-3D, SmarAct), all positions are obtained in the coordinate reference system of this positioning system. The position of the foil can be easily read out. Acquiring the beam parameters of the probe beam and the detector position requires other methods. The beam parameters of a focused Gaussian beam are the waist radius w_0, the Rayleigh length z_R and the offset of the focus in propagation direction z_0. The beam radius along the laser propagation direction z for a Gaussian beam is given by:

$$w(z) = w_0\sqrt{1 + \left(\frac{z - z_0}{z_R}\right)^2} \tag{3.7}$$

These parameters as well as the camera position can by determined by using a *knife-edge* and a *camera* scan. Those methods have already been discussed in multiple bachelor's theses of our group [11, 45, 46]. The methods are used to obtain accurate values for the probe and pump beam parameters and the position of the camera with respect to the foil position.

3.3. Measurement Procedure for the Imaging of Plasma Dynamics

In this thesis, the evolution of the plasma dynamics in laser-excited thin gold foils is studied by coherent diffractive imaging. To successfully image plasma dynamics in thin gold foils, several pieces of information must be obtained during each measurement. This includes the profile of the probe beam, the integrity of the foil, and the shape of the hole after the measurement. The procedure to obtain this data is covered in this section.

In traditional coherent diffractive imaging experiments, only the scattered light of the probe beam is used for the reconstruction [8]. However, our experiment is different in this respect. For a semitransparent target there is not only diffracted light at the position the target is excited, but also light transmitted through the foil outside of the excited area. The transmitted and diffracted light is superimposed on the detector.

As a result a modified phase retrieval algorithm has to be employed to reconstruct the complex electric field at the target position. This phase retrieval algorithm was developed by R. Altenkirch and C. Peltz at the Institute of Physics, University of Rostock in the group of Prof. Fennel: Strong-Field Nanophysics. In this algorithm, the field transmitted through the undisturbed gold foil has to be known accurately, as it is used as a boundary condition in the phase retrieval process. This field is equal to the field that is propagated through the non excited foil and will be called background field from now on.

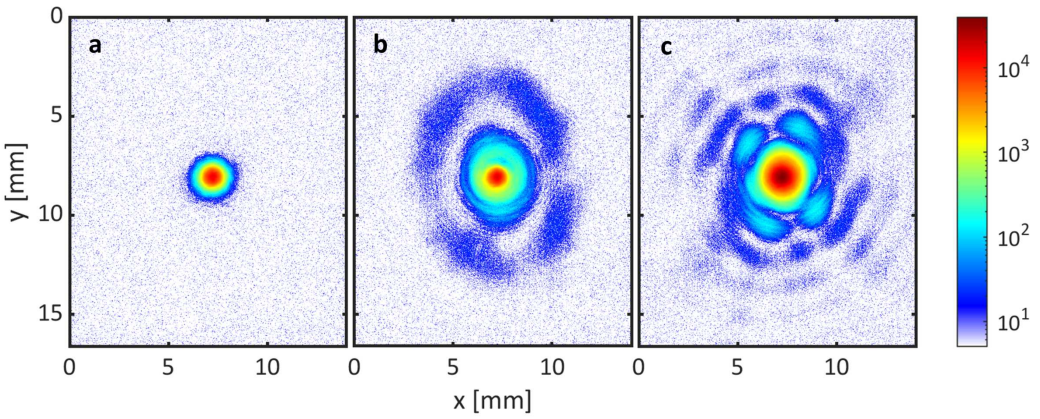

Figure 3.4.: Exemplary illustration of the captured diffraction pictures for each measurement. The *pre* image (**a**) shows the probe pulse transmitted through the undisturbed foil, the *shot* image (**b**) shows the diffraction image obtained $190\,\mathrm{ps}$ after excitation by a $7\,\mu$J pump pulse and the *post* image (**c**) shows the diffraction image of the resulting hole in the foil.

To obtain the background field, the first part of the measurement process is to take the *pre*-image. This is done by blocking the pump pulse with the shutter and recording the probe pulse that is transmitted through the undisturbed gold foil with the CMOS camera. From this image and the beam parameters obtained with the *knife-edge* and *camera* scan, the required background field at the interaction region can be estimated. Furthermore, one can check if the foil is intact at the measurement location by checking, if the *pre* image differs strongly from a Gaussian beam. In Fig. 3.4a, an exemplary *pre* image is shown. The absence of diffraction orders indicates, that the gold foil is intact at the interaction zone. From this image, the background field can be estimated. The second part in the measurement procedure is capturing the so called *shot*-image. In this step, the shutter is opened and one pump pulse excites the gold foil before the shutter is closed again. After an adjustable time delay the probe pulse images the dynamics in the excited foil and the resulting diffraction of the probe pulse is captured by the CMOS camera. These images provide information about the excitation, relaxation, and ablation dynamics in the gold foil. By comparing *shot*-images for different time delays between pump and probe pulse, it is possible to discuss the time evolution of the dynamics in the excited gold foil. An exemplary *shot*-image for a time delay of $190\,\mathrm{ps}$ is shown in Fig. 3.4b.
The third and final captured image in the measurement procedure is the *post*-image. This image is captured a few seconds after the excitation of the foil, when no dynamics are observable anymore. The probe pulse is now diffracted by the hole created in the gold foil. By checking, if the diffraction pattern is symmetric, centered and evenly distributed over the detector, one can determine whether the pump and probe overlap is good. Furthermore, it can be checked if the camera is in adequate distance from the target. The camera is too close to the target if the diffraction orders are confined to the center of the camera and to far away, if diffraction orders are cut of by the edge of the detector. An exemplary *post*-image is shown in Fig. 3.4c.

3.4. Reproducibility of the Excitation and Relaxation Dynamics

In this thesis, the excitation and relaxation dynamics in laser-excited gold foils are studied with single-shot coherent diffractive imaging. To achieve reproducible results it is crucial, that for different time delays, but otherwise unchanged experimental parameters, the same plasma dynamics are induced in the foil. Furthermore, the

spatial overlap and the beam diameter of the pump and probe pulse on the target have to remain constant. Additionally, multiple measurements should yield identical *shot* and *post* images in case the delay time and pump energy are unchanged.
All these conditions require a highly stable setup that is not affected by instabilities in the laser output. A beam stabilization system (Aligna, TEM Messtechnik) is used directly behind the output of the Ti:Sa laser system. This ensures that the laser beam is always coupled into the experiment in the same way with respect to propagation direction and position of the beam. In addition, other sources of instability, such as vibrations of the optical elements, must be eliminated. Consequently, all optics were mounted on fixed-height steel posts with a diameter of 1", which reduces vibration and improves stability compared to adjustable-height posts. The only exception are optics like apertures or the shutter, because the height of those optics is adjusted frequently during the alignment process. However, small vibrations of those optical elements should not affect the beam stability as significantly as the vibration of a lens mount, for example.
In the following sections, the stability of the setup is evaluated using two different methods. First, the reproducibility of the induced plasma dynamics is discussed by examining microscopic images of the holes in the gold foils after the experiment. If the shapes and sizes of the holes are identical regardless of the time delay, this indicates, that the same plasma dynamics were induced for all measurements.
Second, the reproducibility of the imaging of the plasma dynamics is verified. This is done by comparing different *shot*- and *post*-images taken with the same pump energy and pump-probe delay. If the diffraction images are identical, the imaging of the dynamics is also reproducible.

3.4.1. Reproducibility of the Excitation by the Pump Beam

The first method to verify the reproducibility of the excitation of the foil is to compare holes in the foil made at different time delays. If the pulse duration and energy of the pump pulse are not changed, the plasma dynamics in the foil should behave similar. This should ultimately lead to the same holes in the gold foil. To verify whether this condition for a reproducible measurement is met, microscope images of holes in the foil, created with the same pulse energy and duration, but at different time delays, are compared. They are shown in Fig. 3.5 together with the various positions of the delay stage.

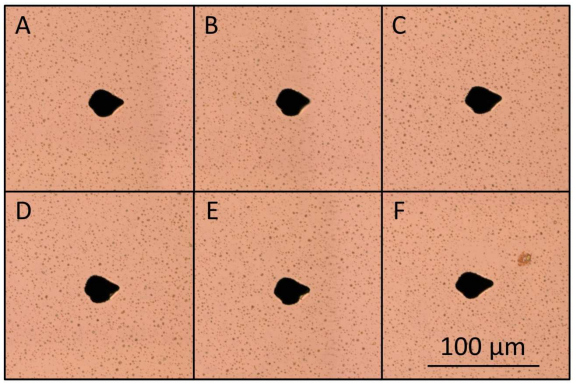

Hole	Position of the delay stage [mm]
A	60.18
B	60.35
C	61.49
D	89.97
E	119.94
F	299.00

Figure 3.5.: Comparison of holes in the gold foil for different positions of the delaystage. **left)** Confocal microscope image of the holes in the gold foil **right)** Positions of the delaystage for the different holes.

Instead of round holes, as one would expect for a Gaussian pump pulse, the holes are asymmetric. While they have a roughly circular form, they feature a distinct spike on the right and a less clear spike on the left. The beam profile of the pump beam can be improved to produce circular holes. This is left for the future. However, all holes, regardless of the position of the delaystage, show the same structure and have similar sizes. This observation indicates, that similar plasma dynamics in the gold foil are induced, regardless of the position of the delay stage. This suggests a stable setup of the pump beam pathway.

3.4.2. Reproducibility of the Imaging of the Plasma Dynamics

In addition to the reproducibility of the induced plasma dynamics, also the imaging of the dynamics by the probe pulse should be reproducible. This includes a fixed spatial overlap of the probe and pump pulse at the target positions for different measurements. One method to check if the imaging of the dynamics is reproducible, is to compare the recorded *post* and *shot* diffraction images for different measurements with the same parameters. Those unchanged parameters are: the excitation energy, the delay time between pump and probe pulse and the pulse duration of the pump and probe pulse. The only change between measurements is the position on the gold foil where the measurements are done.
Two different diffraction images of the *shot* (a, b) and the *post* (d, e) measurement with the same measurement parameters are shown in Fig. 3.6. In addition, the modulus of the difference of both images is given in c for the *shot* and in f for the *post* images. Both *shot* images look qualitative the same. There are no mayor differences in the

diffraction pattern. For both images one can observe a peak in intensity in the middle of the image. Furthermore, there are a few holographic features surrounding this middle peak. The fact that there are no major differences in the diffraction images is confirmed by Fig. 3.6c that shows the modulus of the difference of both *shot* images. The only noticeable deviation of both images is observed in the center of the image where a maximal deviation of around 1000 counts is observed, which is a deviation of less than 10%. As a result, the imaging of the *shot* images seems to be very stable and reproducible.
Both diffraction images obtained during the *post* measurements look qualitative similar to each other as well (see Fig. 3.6 d,e). Both feature a peak in intensity in the center due to the primary beam. Furthermore, multiple diffraction peaks spread outwards with decreasing intensity. The first order diffraction peaks exhibit holographic

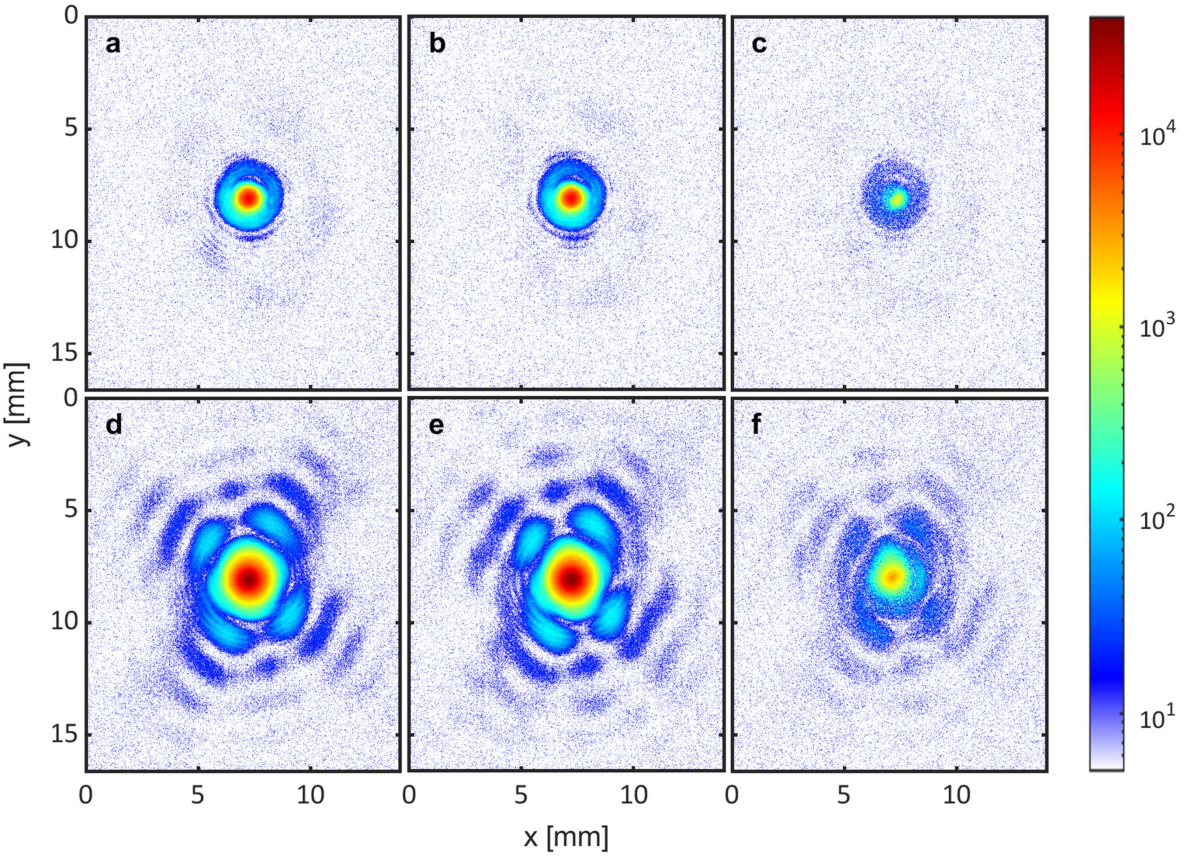

Figure 3.6.: Shot (**a, b**) and post (**d, e**) diffraction images for repeated measurements with the same experimental parameters. The modulus of the difference of both images is given in **c)** for the *shot* and in **f)** for the *post* images. The pump energy was set to $7\,\mu$J and position of the delaystage was $67.49\,\mathrm{mm}$ which corresponds to a time delay of $40.7\,\mathrm{ps}$ between the pump and probe pulse.

features, which are characterized by oscillations overlaying the diffraction peak. Even those fine details do not show significant variation when comparing both images. This is confirmed by Fig. 3.6f that shows the modulus of the difference of both *post* images. The deviation in the center is about 3000 counts. This is a deviation of less than 10%, as the *post* images have about 40000 counts in the same area. A similar relative deviation is observed at regions with fewer counts, for example, the diffraction peaks. As a result, the imaging of the *post* images seems to be very stable and reproducible.
In conclusion, the diffraction images for both the *shot* and *post* measurements are reproducible for multiple measurements. This indicates, that the used setup for the excitation and the imaging of the plasma dynamics is highly stable and different measurements can be compared to each other to achieve a time resolved imaging of the dynamics.

3.5. Thin Foil Characterization

This section is dedicated to the characterization of the target, a $30\,\mathrm{nm}$ thick gold foil. In the experiment the foil is excited by a $800\,\mathrm{nm}$ pump pulse and imaged by a $400\,\mathrm{nm}$ probe pulse after an adjustable delay. The time resolved dynamics in the foil are obtained by comparing measurements conducted at different time delays between pump and probe. However, since the foil is damaged after each measurement, the next measurement with a different delay time between pump and probe pulse has to be done at a different position on the foil. For this method to provide meaningful results, it is crucial that the parameters of the target, such as its thickness, do not change over the area of the foil. To prove that the foil is uniform, this section is dedicated to the characterization of the gold foil.
Measuring the thickness of objects in the vicinity of nanometers, as it is the case for the used gold foils, is challenging, if not impossible, with traditional methods like measuring using rulers, calipers or micrometers, which are typically accurate only down to the micrometer scale at best. Therefore, other measuring methods have to be employed with the goal of measuring the thickness of the foil. Those methods include for example weighing the foil, measuring the energy loss of alpha-particles passing the foil [47] or measuring the strength of electron backscattering [48]. However, those methods have some drawbacks. For e.g., if the foil is weighed, one can only obtain the average foil thickness but no spatial resolved thickness. Furthermore, a high-precision scale is required since a $30\,\mathrm{nm}$ thick and $1\,\mathrm{cm}$ wide gold foil only weighs about $60\,\mu\mathrm{g}$. Measuring with alpha and beta particles requires dedicated setups.

The method of choice in this thesis is the indirect measurement of the foil thickness by measuring the transmittivity of the gold foil for the $400\,\mathrm{nm}$ probe beam at different positions on the foil. As discussed in chapter 2.1.1, the transmittivity only depends on the thickness of the film, the refractive index of the material and the wavelength. It is given by the following relation:

$$T = \frac{I_T}{I_0} = \left| t_1 t_2 e^{\mathrm{i}kL} e^{-\alpha L} \cdot \frac{1}{1 - (r \cdot e^{-\alpha L} e^{\mathrm{i}kL})^2} \right|^2 \tag{3.8}$$

Since the wavelength is known, the transmittance can be measured, and literature values are available for the refractive index, the thickness of the foil can be extracted. This method can be easily incorporated into the existing setup and allows for a spatial resolved foil thickness measurement.

In Fig. 3.7a the measured transmittance of a thin gold foil used in this thesis is shown. One can see that the transmittance experiences strong deviations in some small ($<100\,\mu\mathrm{m}$) spots (e.g. see arrows in Fig. 3.7a) where the transmission drops roughly $1\,\%$ below the mean transmission of the foil. Furthermore, an artifact is observable with spots and lines where the transmission drops below the mean transmission (see dashed circle). The area surrounding this artifact has a transmission higher than the mean. Apart from those exceptions the transmittance only varies slightly over the whole area of the foil.

To retrieve foil thickness map corresponding to the transmission map, the foil thickness is calculated by solving eq. 3.8 for L numerically. The resulting thickness map is shown in Fig. 3.7 b). The refractive index used for the calculation was taken from

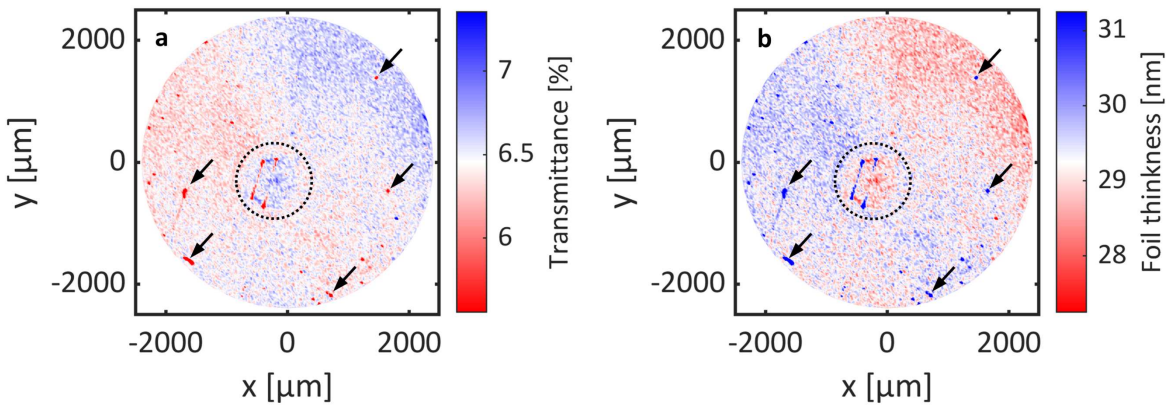

Figure 3.7.: a) spatial resolved measured transmittance and **b)** calculated foil thickness using the procedure discussed in the text with the refractive index for gold given in [13].

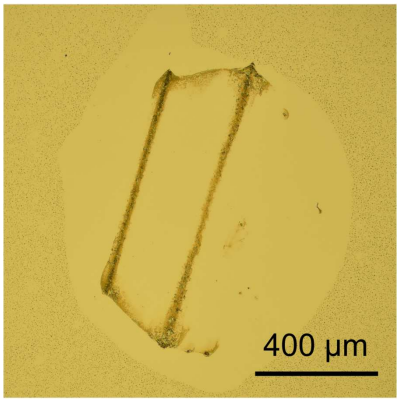

Figure 3.8.: Optical microscope image of the area on the gold foil marked with a dashed circle in Fig. 3.7. The artifact is clearly visible at the center, featuring darker lines surrounded by a circle that is slightly lighter in color than the rest of the foil.

[13]. The average thickness is $L = 29.25\,\mathrm{nm}$ which is close to the value given by the manufacturer of $L = 30\,\mathrm{nm}$.
As indicated by the arrows, the same spots where a lower transmission was observed, a larger foil thickness was calculated. The same can be seen for the artifact (see dashed circle). The low transmission spots and lines result in a large foil thickness, whereas the high transmittance surrounding results in a thinner foil thickness.
To investigate the observed artifact further, the area marked by a dashed circle in Fig. 3.7 was viewed using an optical microscope. A picture of the artifact is shown in Fig. 3.8. One can clearly see a structure with the same shape as the artifact observed in the transmission measurement. Furthermore, the color of the gold foil near the structure differs from the color of the rest of the foil. This area was also conspicuous in the transmission measurement and showed itself in an increase in transmission. One can only speculate about the cause for this structure to appear in the manufacturing process. However, since this artifact is spatially confined and well visible in the transmission measurement as well as under the microscope, it should not be a problem in the experiment, as measurements near this defect can be easily identified and discarded. Furthermore, they can be sorted out by looking at the *pre* image of each measurement. If one *pre* image differs greatly from the others, this indicates that the film may be damaged at the point where the measurement was taken. Other areas on the foil where a homogeneous transmission profile was observed showed no conspicuous features under the microscope.
In conclusion, the studied foil only shows small deviations in thickness over the whole area. However, in some places strong deviations from the mean thickness can be observed. Measurements taken in those areas have to be discussed with care or be discarded entirely. Overall, however, the films are well suited for the experiment and allow for time resolved measurement by comparing measurements from different positions on the foil.

Chapter 4.

Excitation and Relaxation Dynamics in Laser-Excited Thin Gold Foils

Now that the methods necessary for the imaging of the plasma dynamics have been presented, this chapter is dedicated to the analysis of the plasma dynamics in the laser-excited thin gold foils. The $30\,\mathrm{nm}$-thick free-standing gold foils are excited by a focused femtosecond (fs) $800\,\mathrm{nm}$ pump pulse with adjustable pulse energy and polarization. The excited foil is subsequently imaged by a low intensity fs-400 nm pulse with variable time delay up to 2 ns. Information about the plasma dynamics is extracted from the diffraction images of the probe beam.

In the first part, the dependence of the plasma dynamics on the pump intensity and polarization is discussed by analyzing the diffraction images in terms of the total captured probe intensity and the structure of the diffraction patterns for different time delays and pump pulse parameters. Furthermore, the ablation threshold of the gold foil is determined by viewing holes in the foil shot with different energy densities under a microscope. In the second part, a phase retrieval algorithm developed by R. Altenkirch and C. Peltz is used to reconstruct the electric field at the foil position. From the reconstructions, information about the plasma dynamics in the gold foil is obtained.

4.1. The Influence of Laser Parameters on the Evolution of the Plasma Dynamics

4.1.1. Change in the Transmission of a Gold Foil Excited by an Ultrashort Laserpulse

A simple but powerful method to study plasma dynamics in thin gold foils after excitation by an ultrashort laser pulse is the analysis of the time resolved transmission. The time resolved transmission is calculated by normalizing the total captured intensity of the *shot* image by the total intensity of the *pre* image.
The time dependent transmissions for three different pump pulse intensities are shown on the left side in Fig. 4.1. For time delays less than zero, i.e. for the probe pulse imaging the foil before the pump pulse excites it, the transmission is constant at 1. This can be easily understood, since for negative time delays the probe pulse only probes the undisturbed foil when measuring the *shot* image. Because the intensity is normalized by the *pre* image, the result must be a transmission of 1. The small

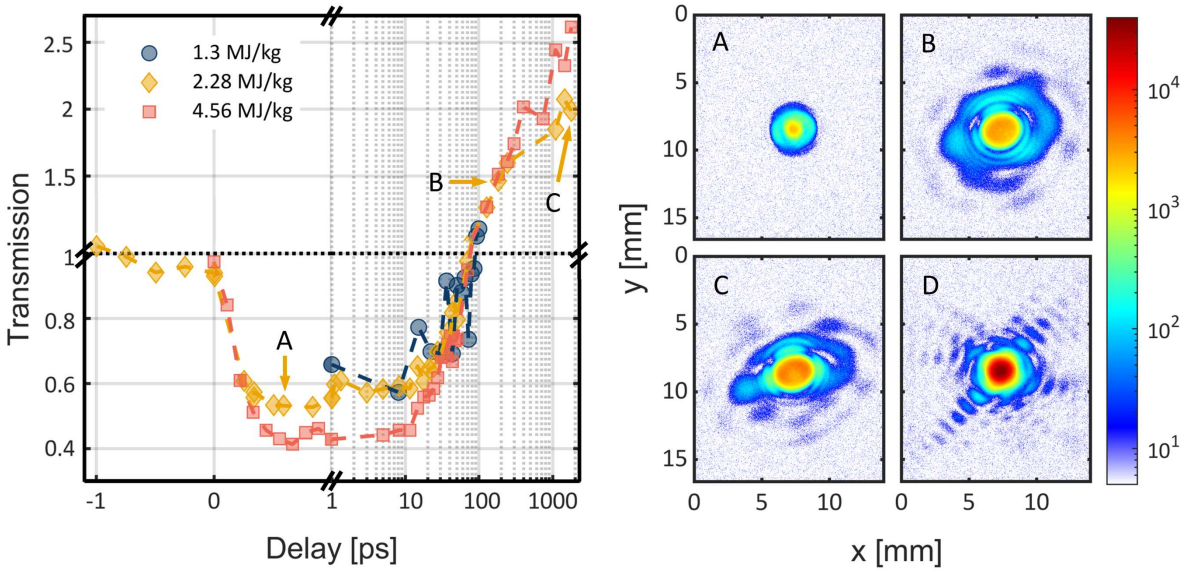

Figure 4.1.: left) Time-dependent transmission curves for three different (1.3, 2.28 and 4.56 $\mathrm{MJ\,kg^{-1}}$) absorbed energy densities. Only the energy of the pump pulse has been adjusted between measurements by turning the first polarizer in the pump beam path. The x-axis is linear until $1\,\mathrm{ps}$ and then logarithmic. The scaling of the $y-$axis below and above 1 differs. **right)** Four selected diffraction images from the measurement with a pump peak intensity of $2.28\,\mathrm{MJ\,kg^{-1}}$ for time delays of **A)** $0.59\,\mathrm{ps}$, **B)** $185\,\mathrm{ps}$, **C)** $1800\,\mathrm{ps}$ and **D)** ∞ (post image for the measurement shown in C)

deviations from a transmission of 1 can be explained by a shot-to-shot pulse energy variations of the laser, which leads to slightly different probe intensities for the *pre* and *shot* measurement and ultimately to small variations in the transmission. The transmission varies in an interval between 0.94 and 1.02, underlining the high stability of the setup.

For time delays between $0\,\mathrm{ps}$ and $0.7\,\mathrm{ps}$, the transmission is drastically reduced to about 0.55 and 0.45 for pump intensities of $2.28\,\mathrm{MJ\,kg^{-1}}$ and $4.46\,\mathrm{MJ\,kg^{-1}}$, respectively. The transmission then stays nearly constant until $10\,\mathrm{ps}$, where an increase in transmission is observed. In addition, for the pump intensity of $1.3\,\mathrm{MJ\,kg^{-1}}$, the transmission is less than 1 at $1\,\mathrm{ps}$ and increases as well after about $10\,\mathrm{ps}$. However, there were no measurements made in the first ps for this pump intensity, because there was not enough space left on the gold foil to measure at all time delays measured in the other measurement series.

The decrease in transmission can be explained qualitatively by the Drude Model. The pump pulse energy is absorbed by the electrons in the gold foil. This leads to an increase in the free-electron density n_e and, consequently, the plasma frequency ω_p rises. The plasma frequency describes the maximal frequency at which the electrons can still follow an incoming electric field. As the electrons are oscillating with the same frequency as the incoming electric field they reflect it as a result. For that reason, an increase in the plasma frequency leads to a higher reflection and ultimately to a reduction of the transmission.

From the measurements shown in Fig. 4.1, it appears that the transmission for a time delay between 0.7 and $10\,\mathrm{ps}$ decreases more for larger pump pulse intensities. This effect will be discussed in more detail later, as the general shape of the curves will be discussed first.

For time delays exceeding $10\,\mathrm{ps}$, the transmission increases again for all three different pump intensities (see Fig. 4.1) and after roughly $100\,\mathrm{ps}$ the transmission reaches values larger than one and is higher compared to the non excited foil.

The increase in transmission after $10\,\mathrm{ps}$ can be explained using the TTM (see section 2.1.2). After the electrons are excited, which can be described as an increase in electronic temperature, the electrons transfer their heat to the lattice. This results in the electronic temperature decreasing and the lattice temperature increasing. This energy transfer from the electrons to the lattice leads to a reduced excitation of the electrons and, therefore, to a reduced free-electron density, increasing the transmission. The characteristic time of this energy transfer is on a time scale of some $10\,\mathrm{ps}$. This is in agreement with the recorded data, as the transmission increases after a similar time

delay. Furthermore, some excited electrons might leave the foil, which also leads to a reduced free electron density

However, the increase in transmission can be explained by a second effect, namely the onset of lattice dynamics in the gold foil. Since the lattice is heated due to energy transfer from the electronic system, the now heated lattice is melting and subsequently expanding due to a pressure buildup in the foil [30]. As the thickness of the created plasma increases, the electron density is reduced during this process. This leads to a reduced reflection and, as a result, to an increase in transmission.

The TTM as well as the literature suggest melting of the foil after $10\,\mathrm{ps}$ for an absorbed energy density larger than $1\,\mathrm{MJ\,kg^{-1}}$ [30]. Since the used energy densities in Fig. 4.1 lie in the range of $1.3\,\mathrm{MJ\,kg^{-1}}$ to $4.6\,\mathrm{MJ\,kg^{-1}}$, the lattice dynamics should start after roughly $10\,\mathrm{ps}$ resulting in an expansion of the excited foil. This leads to an increase in transmission after about $10\,\mathrm{ps}$.

However, as the cooling of the electronic system and the lattice ablation dynamics both overlap in time and both result in an increase in transmission, it is difficult to extract the exact time at which the expansion of the excited foil begins from the transmission curve alone.

Fig. 4.1 shows, that the transmission exceeds 1 after $100\,\mathrm{ps}$ for all three energy densities used. Without expansion, the electron density would not drop below the level in the undisturbed foil, so the transmission would not surpass 1. As a result, the foil has to be expanding at a time delay of $100\,\mathrm{ps}$.

However, apart from the heating of the lattice system and the subsequent expansion due to the ion dynamics, a Coulomb explosion could lead to ablation and an increased transmission as well. A Coulomb explosion occurs when a target is rapidly ionized, for example by an intense, ultrashort laser pulse. This leads to repulsion and subsequent disintegration of the now positively charged ions. Coulomb explosions have been thoroughly studied for example on molecules or clusters [36]. Studies for thin metal films suggest, that Coulomb explosion has to be considered only for laser fluences close to the ablation threshold, i.e. for ablation depths below $20\,\mathrm{nm}$. For larger energy densities the dominant effect is the thermal ablation [37]. As the used foils are $30\,\mathrm{nm}$ thick and clear holes where observed under the microscope, thermal ablation is most likely the dominant effect that leads to ablation. However, the Coulomb explosion mechanism might be important to describe the ablation dynamics at the edges of the excited region, since the laser intensity is close to the ablation threshold in this area.

To examine if the transmission reaches values of 1 after $100\,\mathrm{ps}$ for other energy densities as well, the transmission $100\,\mathrm{ps}$ after excitation was measured for different energy

densities. The result will be addressed after the general shape of the transmission curves was discussed completely.

Given that an increase in transmission is observed after $10\,\mathrm{ps}$ and a transmission above 1 after $100\,\mathrm{ps}$ for the utilized energy densities, it can be reasoned that the onset of lattice dynamics must occur between 10 and $100\,\mathrm{ps}$. The expansion of the excited foil then leads to a further increase in the transmission with increasing time delay. At $1800\,\mathrm{ps}$, which marks the maximum time delay with the current setup, the transmission reaches values of 2 and 2.5. The average transmission of the *post* measurements is 5.8 and 6.1 (not shown in Fig. 4.1) for pump intensities of $2.28\,\mathrm{MJ\,kg^{-1}}$ and $4.56\,\mathrm{MJ\,kg^{-1}}$, respectively. As the curves do not reach the *post* transmission values and as they are not flattened at a time delay of $1800\,\mathrm{ps}$, one can conclude that the dynamics in the foil are not finished even $1800\,\mathrm{ps}$ after the excitation. This is underlined when comparing the *shot* (C) with the *post* (D) image in Fig. 4.1. One can still see major differences between both images, which confirms that the imaging time of about $2\,\mathrm{ns}$ is too small to resolve all the dynamics in the foil.

In order to resolve the whole ablation process, a longer maximal time delay is needed. This could be achieved in the future by going through the delay stage a second time, improving the maximum time delay by a factor of 2 to about $4\,\mathrm{ns}$.

After discussing the general course of transmission as a function of time delay, the energy dependence of transmission at characteristic time delays is examined. As mentioned above, the transmission in the first $10\,\mathrm{ps}$ seems to decrease more for higher pump energies. To verify this observation, a second measurement was performed. For this measurement, the time delay between pump and probe pulse was set to $5\,\mathrm{ps}$ and a variety of pump pulse energies were used to excite the gold foil. The delay of $5\,\mathrm{ps}$ was chosen, because it is about halfway between the decrease and the increase of the transmission. The transmission at a time delay of $5\,\mathrm{ps}$ for a variety of pump pulse energies is shown in Fig. 4.2. The $x-$axis shows the energy density used for the excitation of the foil and the $y-$axis shows the transmission of the gold foil after a time delay of $5\,\mathrm{ps}$.

As already suspected from Fig. 4.1, the transmission decreases with increasing pump intensity. The smallest transmission value 0.46 is measured at the highest energy density of $7.19\,\mathrm{MJ\,kg^{-1}}$. The descent of the transmission with intensity seems to be approximately linear. However, the transmission can not reach values below zero. Therefore, the course of the graph is expected to flatten for even higher intensities. Unfortunately, there were no measurements done for energy densities surpassing $7.19\,\mathrm{MJ\,kg^{-1}}$. Con-

sequently, the course of the graph for higher energy densities has to be measured and discussed in the future.
As before, the decrease in transmission with increasing pump intensity can be qualitatively explained by the Drude model. With increased pump intensity, more electrons are excited, leading to an even higher free electron density. This leads to a higher reflectivity and, as a result, to a lower transmission with increasing pump intensity. However, more sophisticated theoretical models are required to quantitatively explain the course of the graph, such as the linear decrease.
In addition to the increased excitation, the size of the holes and thus the excited area increases with increasing pump pulse energy. Since a larger area is excited, a larger area contributes to the decrease in transmission. This overlays the effect due to the increased free electron density in the center. However, the increase in the hole size for a Gaussian pump beam should proportional to the logarithm of the pump laser energy [49]. If the decrease in transmission were due only to the increasing size of the excited area, no linear decrease of the transmission as a function of the pump energy would be observed. Therefore, the transmission decrease is at least partially due to the increased excitation in the center of the excited region.
To separate the decrease in transmission due to a higher excitation in the center from the decrease due to a larger excited region, reconstructions of the complex transmission are needed.
Note, that the transmission does not reach 1 even at energy densities of $0.5\,\mathrm{MJ\,kg^{-1}}$, although no ablation was observed at these intensities (see microscope image in Fig. 4.2). As we see no ablation, the lattice should be almost undisturbed at these intensities, but since we see a reduced transmission at a time delay of $5\,\mathrm{ps}$, the electronic

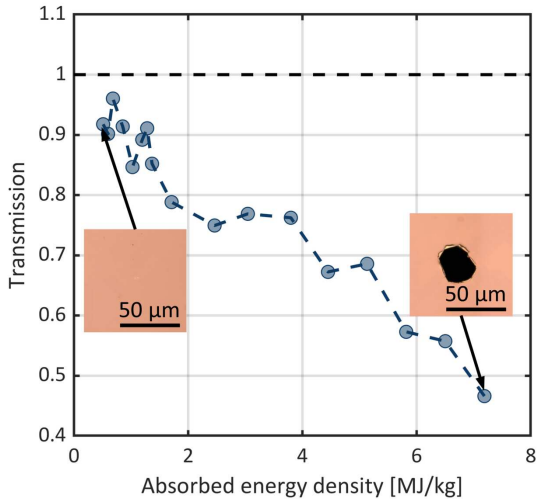

Figure 4.2.: Transmission for a pump-probe time delay of $5\,\mathrm{ps}$ as a function of the absorbed energy density. The pump pulse energy has been adjusted by turning the first polarizer in the pump beam path. Two exemplary microscope images are shown for the minimal and maximal pump intensity.

subsystem must be responsible for the change in transmission on such timescales. Since we see a separation of electron and lattice dynamics, this further underlines that the Two-Temperature-Model (TTM) that was discussed in section 2.1.2 is applicable here and only the electrons have to be discussed in the first $10\,\mathrm{ps}$ after excitation.
Another notable point in the transmission curve as a function of time delay occurs at $100\,\mathrm{ps}$. At this time delay, the transmission reaches a value of 1 in Fig. 4.1, independent of the pump energy used. To examine this observation further, the time delay was set to $100\,\mathrm{ps}$ and the transmission is measured in dependence of the pump pulse energy.
The transmission at a time delay of $100\,\mathrm{ps}$ for a variety of pump pulse energies is shown in Fig. 4.3. The $x-$axis shows the absorbed energy density and the $y-$axis shows the transmission of the gold foil after a time delay of $100\,\mathrm{ps}$.
As already suspected from Fig. 4.1, the transmission $100\,\mathrm{ps}$ after excitation is approximately 1 for all used energy densities. Only three out of 16 measurements deviate more than 10% from a transmission value of 1. There is no clear trend visible on how the transmission changes with increasing pump energy.
For a time delay of $5\,\mathrm{ps}$, a decrease in transmission was observed for higher excitation energies. This was assigned to an increased free electron density, which increased reflection and thus decreased the transmission. The rise in transmission after about $10\,\mathrm{ps}$ was assigned to the onset of lattice dynamics which lead to an expansion of the excited foil and, as a result, to a reduction of the free electron density.
Since transmission reaches 1 across all energy levels after $100\,\mathrm{ps}$, it is likely that higher excitation, which initially reduces transmission in the first few picoseconds, accelerates the expansion of the plasma induced in the excited gold foil. At $100\,\mathrm{ps}$, the reduced transmission due to the increased excitation was presumably compensated by

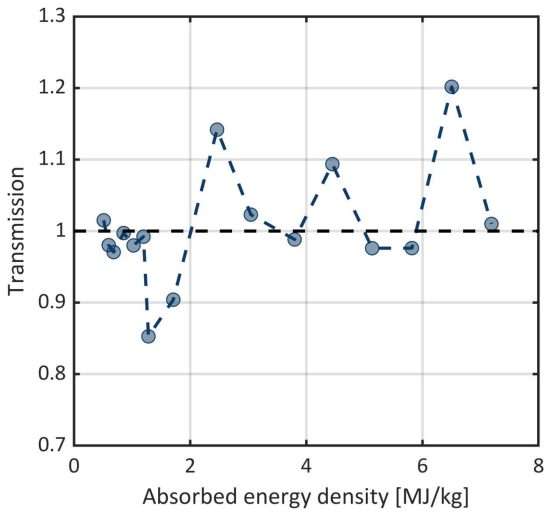

Figure 4.3.: Transmission for a pump-probe time delay of $100\,\mathrm{ps}$ as a function of the absorbed energy density. The pump pulse energy has been adjusted by turning the first polarizer in the pump beam path.

the increased transmission due to the faster expansion of the foil. Therefore, this measurement could indicate a faster expansion speed of the excited gold foil for higher excitation energies. However, this observation will have to be proven or disproved in the future by analyzing reconstructions of the electric field at the target position for different pump energies and time delays.
In summary, the time-dependent transmission curves provide information about the time scales of various processes in the foil. These include the excitation of electrons in the first few hundred fs, the melting and expansion of the gold foil after about $10\,\mathrm{ps}$ to $100\,\mathrm{ps}$, and finally the ablation of the material that is still ongoing after more than $2\,\mathrm{ns}$. However, one can see in Fig. 4.1, that in addition to the total intensity, the structure of the diffraction images changes greatly with the time delay. Hence, the structure of the captured diffraction images may hold more information than the total intensity alone. For that reason, the next section is dedicated to the analysis of the change in the structure of the diffraction images for different time delays.

4.1.2. Analysis of the Diffraction Pattern Shape Evolution

In this section, the evolution of the structure of the diffraction images is analyzed. One common method visualize the structure change of diffraction images as a function of the time delay is to analyze the evolution of the average intensity along an axis with multiple diffraction orders. The coordinate system is illustrated in Fig. 4.4. To reduce the influence of noise, especially far from the center where the intensity of the diffraction orders decreases, the intensity at each distance r from the center is averaged over the opening angle dθ and a radial step dr. It should be noted, that the size radial step dr is greatly exaggerated in Fig. 4.4 for a better visualization. It is set to rather small values of 2 pixels which corresponds to $13\,\mu\mathrm{m}$.
The origin $\mathcal{O}$ is set to the center of the diffraction image, which is the middle of the captured probe beam profile in the *pre* image. The center position is calculated by applying a Gaussian filter to smooth the diffraction image and then peak position is located for this smoothed image. This ensures that the origin $\mathcal{O}$ is always set to the center of the diffraction image and that noise does not cause the origin to be set incorrectly.
Afterwards, the average measured counts are calculated in each of the area elements dA. The result is an average intensity along the angle θ as a function of the distance from the center r. To observe the structural change of the diffraction patterns with time, this procedure is done for *shot* measurements at different time delays and plotted

as a false-color image where the x-axis is the time delay, the $y-$axis is the distance from the center r and the average intensity is represented by the color with logarithmic scaling.

The structure evolution should be best visible for an angle θ where multiple diffraction orders are observed. As a consequence the angle θ is set in a direction with many diffraction orders and the opening angle dθ is set in a way that the total width of the diffraction maxima is captured. The angles used are $\theta = 42°$ and d$\theta = 10°$

Figure 4.5 shows two images obtained using the procedure described above. The $x-$axis is linear until $1\,\mathrm{ps}$ and then logarithmic. The used excitation energies are $2.28\,\mathrm{MJ\,kg^{-1}}$ and $4.56\,\mathrm{MJ\,kg^{-1}}$ for picture a) and b), respectively.

In the first picosecond after excitation, the width and maximal intensity of the primary beam decreases for both excitation intensities. However, the effect is greater for the larger excitation energy of $4.56\,\mathrm{MJ\,kg^{-1}}$ in Fig. 4.5b.

Moreover, multiple diffraction orders appear after roughly $0.5\,\mathrm{ps}$. This is identified by the intensity oscillating in the r-direction. The oscillations are spatially confined to about $3\,\mathrm{mm}$ and $4\,\mathrm{mm}$ from the center for $2.28\,\mathrm{MJ\,kg^{-1}}$ and $4.56\,\mathrm{MJ\,kg^{-1}}$, respectively. Since this structure does not change until about $10\,\mathrm{ps}$ after excitation, it indicated that there is no drastic change in the refractive index of the foil and as a result, most likely no expansion of the foil in this time. The reduction of intensity in the central part of the image can be explained in the same manner as in section 4.1.1: The pump laser excites the electrons in the foil, leading to a increase in reflection and, therefore, decrease in transmission.

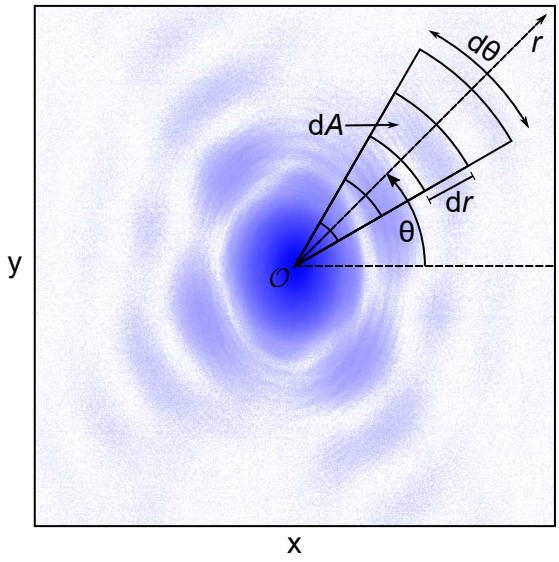

Figure 4.4.: Sketch of the coordinate system used to bin the captured intensity along an angle. Furthermore, an exemplary diffraction image is shown.

Now the reason for the observed structure of the diffraction images, in particular what causes the diffraction orders to be spatially confined to the center of the image during the first $10\,\mathrm{ps}$, shall be discussed.
As the ionization rate is dependent on the local intensity of the pump pulse, the ionization rate should follow the pump pulses lateral intensity profile. This leads to an increased electron density in the center of the excited region and an unchanged electron density far away (in the lateral direction) from the center. Because the intensity profile of the pump beam is continuous and not step-like in lateral direction, there is a continuous transition from high to low electron density. Therefore, also the refractive index changes continuously over the extend of the excited area.
To unravel the features in the diffraction pattern that are caused by an continuous refractive index profile, the diffraction image is calculated for a step-like change of refractive index and a continuous change of the refractive index. The masks used for the computation and the simulated diffraction images are shown in Fig. 4.6. The diffraction images are calculated using the angular spectrum method. The diffraction image of the object with a step like change in the refractive index (hard edge) results in multiple diffraction orders that spread far outward. For the diffraction of the object with a continuously changing refractive index (soft edge), only few diffraction orders that are spatially confined to the center can be seen.
This is because the structure of the image in the far field is related, to a good approximation, to the Fourier transformation of the field behind the diffracting object [50]. If

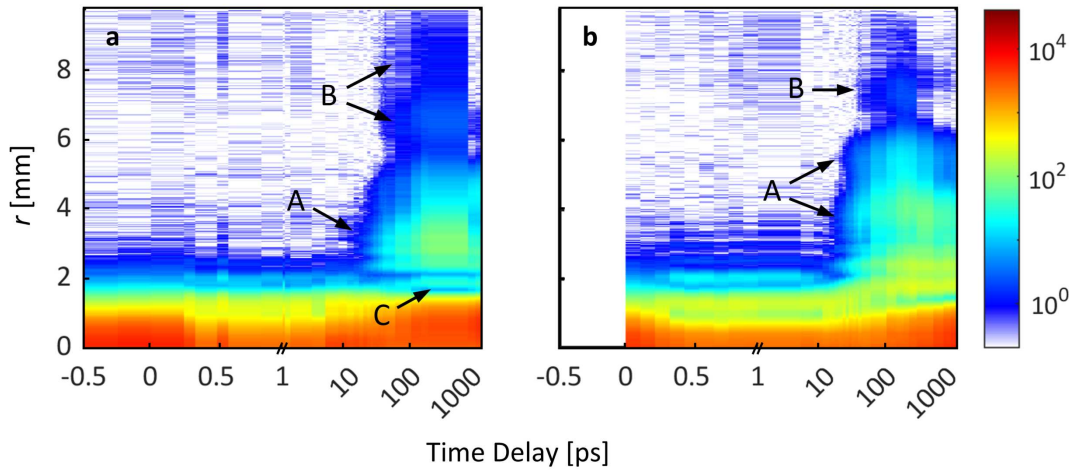

Figure 4.5.: Time resolved angle binned *shot* diffraction images. The time axis is linear until $1\,\mathrm{ps}$ and logarithmic for longer time delays. The angles are set to $\theta = -42°$ and $\mathrm{d}\theta = 10°$. The pump energy densities are **a)** $2.28\,\mathrm{MJ\,kg^{-1}}$ and **b)** $4.56\,\mathrm{MJ\,kg^{-1}}$. Since no measurements were taken for time delays below 0 for the measurement in b), this region was left blank.

the object is smooth, i.e. the refractive index has no jumps, this leads to a diffraction image with few diffraction orders. However, if there are edges in the diffracting object, as it is the case for the *post* images, this leads to multiple diffraction orders extending outwards to the edge of the detector.
This underlines the argument, that in the first few picoseconds after excitation there are no jumps in the complex refractive index at the object position, since the change in electron density follows the pump beam profile. Thus, the lattice dynamics in the foil most likely have not started, as this would cause a step-like change in refractive index at the crossover point where just enough energy is absorbed for the onset of lattice dynamics.
In Fig. 4.5, it can be seen, that the structure of the diffraction images changes drastically after about $15\,\mathrm{ps}$ for both pump intensities. However, the change in the diffraction images is different for both intensities. For a absorbed pump energy density of $2.28\,\mathrm{MJ\,kg^{-1}}$ (a), at first only one widespread diffraction order that is overlayed by multiple oscillations appears about $3\,\mathrm{mm}$ from the center after $15\,\mathrm{ps}$ (see arrow A). The width of the diffraction peak broadens with increasing time delay and the oscilla-

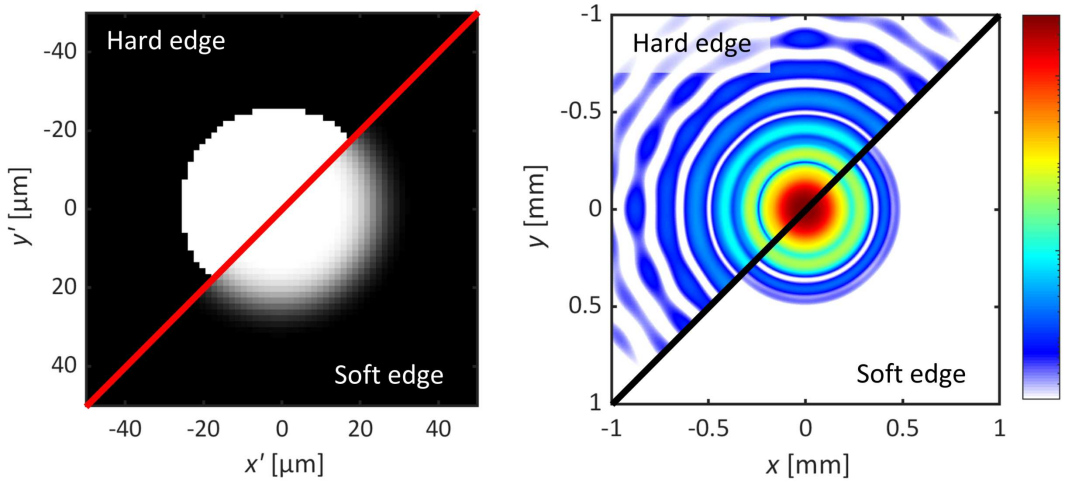

Figure 4.6.: left) The mask used for the diffraction of a Gaussian beam and **right)** the resulting diffraction image $2\,\mathrm{cm}$ behind the foil. The mask shows values between 0 (white) and 1 (black) that are multiplied with the complex refractive index of gold to receive the refractive index distribution which diffracts the Gaussian beam. The foil is set to a thickness of $30\,\mathrm{nm}$ and the beam is propagated using the angular spectrum method. The shown images were obtained from two different numerical calculations and were combined for a better visualization. The top left of the images show the mask and the corresponding diffraction image for a hole with a clearly defined edge (hard edge). The bottom right part of the images show the mask and the diffraction image for the same mask, but with the edge smoothed using a Gaussian filter (soft edge).

tions seem to disappear. At $40\,\mathrm{ps}$, two new diffraction orders appear about $6.5\,\mathrm{mm}$ and $8.5\,\mathrm{mm}$ from the center with lower intensity (see arrow B). The diffraction minima are positioned at $5.8\,\mathrm{mm}$ and $7.8\,\mathrm{mm}$. After about $200\,\mathrm{ps}$, an additional feature arises. One can observe a small peak near the primary beam (see arrow C).
For the measurement with higher pump pulse energy ($4.56\,\mathrm{MJ\,kg^{-1}}$, Fig. 4.5b), the change in structure is different. After $15\,\mathrm{ps}$ two diffraction orders appear roughly $4\,\mathrm{mm}$ and $5.5\,\mathrm{mm}$ from the center (see arrow A). After $40\,\mathrm{ps}$ a third diffraction peak appears (see arrow B). Furthermore, the first two peaks seem to merge into one wide feature over time.
As discussed above, if multiple diffraction orders far from the primary beam are observed, this means that the refractive index of the diffracting target changes step-like in lateral direction. This sudden change in the refractive index could be located right at the crossover point where just enough energy for an expansion of the foil was absorbed. This leads to multiple diffraction orders extending far away from the primary beam. Because the diffraction orders far away from the center are formed after $15\,\mathrm{ps}$ for both pump intensities, we can conclude that the lattice dynamics in the foil seem to start about $15\,\mathrm{ps}$ after excitation. However, the small features observed in the evolution of the structure of the diffraction images cannot be interpreted as easily. Thus, the reconstructed electric field at the target position is needed for a detailed analysis of the plasma dynamics.
In conclusion, the results obtained in section 4.1.1 were confirmed by analyzing the change in the structure of the diffraction images. However, the time delay at which the lattice dynamic sets in has been determined with greater precision: The lattice dynamics in the foil seem to set in around $15\,\mathrm{ps}$ after the excitation, regardless of the pump intensity used. However, the time at which the lattice dynamics set in may vary if the excitation energy is varied over a wider range.

4.1.3. Ablation Threshold of Thin Gold Foils

An important parameter when discussing the dynamics in laser excited media is the ablation threshold. It describes the minimum laser energy required to remove material from a substrate. This section aims to determine the ablation threshold of a thin gold foil when excited by an $800\,\mathrm{nm}$ femtosecond pump pulse. It is then compared with the ablation thresholds obtained in other studies.
Figure 4.7 shows holes in the gold foil that were shot with different pump pulse energy densities ranging from $0.51\,\mathrm{MJ\,kg^{-1}}$ to $7.19\,\mathrm{MJ\,kg^{-1}}$. The holes get larger with increas-

ing pump energy. Additionally, the structure of the holes varies with the used pump pulse energy. For absorbed energy densities of $0.86\,\mathrm{MJ\,kg^{-1}}$ and $1.37\,\mathrm{MJ\,kg^{-1}}$ the holes are shaped like ellipses with the major axis orientated from left to right. However, the shapes get irregular for higher energy densities. Moreover, the edges of the holes shot with energy densities of $5.14\,\mathrm{MJ\,kg^{-1}}$ and $7.19\,\mathrm{MJ\,kg^{-1}}$ seem to bend out of the foil plane. The irregular structures may be due to a pump beam profile that deviates slightly from an ideal Gaussian beam profile.

A common method to determine the ablation threshold of thin foils is to measure the hole size as a function of laser fluence. The size of the hole created by a Gaussian laser pulse is given by [49]:

$$D^2 = 2w_0^2 \ln\left(\frac{\phi_{\mathrm{pk}}}{\phi_{\mathrm{th}}}\right) \tag{4.1}$$

Here, D denotes the diameter of the created hole, w_0 is the $1/e^2$ radius of the Gaussian beam and ϕ_{pk} and ϕ_{th} are the peak laser fluence and ablation threshold fluence, respectively. As the fluence is proportional to the energy density if the beam parameters

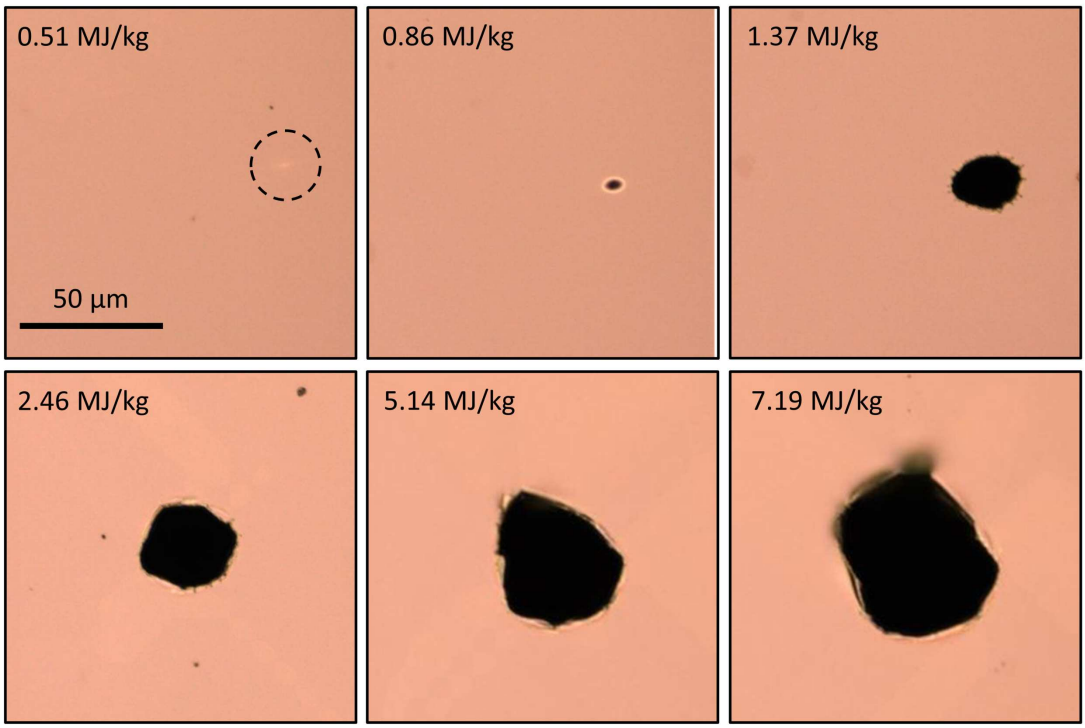

Figure 4.7.: Six exemplary holes in the gold foil shot with different pump pulse energies. The peak absorbed energy density is shown in the top left in each image. For an energy density of $0.51\,\mathrm{MJ\,kg^{-1}}$ no hole was created, but the color of the foil change to a slightly brighter tone in one spot (see dashed circle).

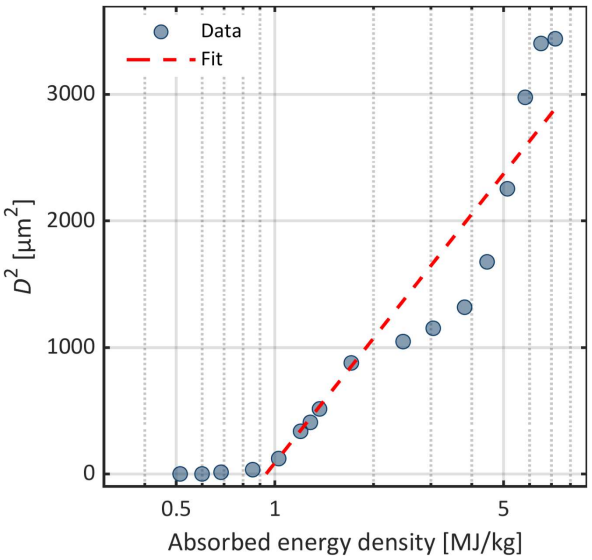

Figure 4.8.: The square of the hole diameter D^2 as a function of the absorbed energy density. The fit function is given in the text. The ablation threshold is the intersection of the fit with $D^2 = 0$.

are unchanged, ϕ_{pk} and ϕ_{th} can be replaced by the absorbed energy density and the ablation threshold energy density.

By giving the square of the hole diameter as a function of the natural logarithm of the energy density used, the ablation threshold can be obtained using linear regression. The intercept at $D^2 = 0$ is the ablation threshold.

The hole diameter used for the fit is the average of the width and height of the holes. The width and height were determined using confocal microscope images of the foil. The squared hole diameter as a function of the absorbed energy density is given in Fig. 4.8. Only the measurements where a hole was created ($D^2 > 0$) are used for the fit. The fit is in good agreement for the energy densities between $1\,\text{MJ}\,\text{kg}^{-1}$ and $2\,\text{MJ}\,\text{kg}^{-1}$. However, the deviation from the fit increases for higher energies. A reason for this observation could be the irregular structure of the holes shot with high pump energy. This may invalidate the method of obtaining the diameter of the holes by calculating the average of the width and height.

Nonetheless, the ablation threshold was determined from the fit. It is the energy density at which the fit intersects $D^2 = 0$. The single shot ablation threshold for gold was determined to be $0.9 \pm 0.3\ \text{MJ}\,\text{kg}^{-1}$. Other studies found ablation thresholds for gold foils with similar thickness to be in the range of $0.33\,\text{MJ}\,\text{kg}^{-1}$ to $1\,\text{MJ}\,\text{kg}^{-1}$ [30, 51, 52]. The results obtained are therefore in agreement with other studies. One strategy to reduce the measurement uncertainty in the future, is to improve the beam quality of the pump beam. This should result in circular holes in the foil.

4.1.4. Polarization Dependence of the Plasma Dynamics

After the dependence of the pump beam energy on the plasma dynamics was discussed in the last sections, this section is dedicated to the influence of the pump pulse polarization on the induced dynamics in the foil. Other research groups have already studied the polarization dependence on the ablation dynamics for insulators and thin metal films on a quartz substrate and an elongation of the created holes along the polarization axis has been observed in both material classes [53, 54]. However, for metals this elongation was only observed for pump energies close to the ablation threshold.
To analyze the impact of the pump pulse polarization on the plasma dynamics in thin, free standing gold foils, two measurements are made with the same pump energy but different pump polarizations. The polarization of the pump pulse is adjusted using the second polarizer in the pump beam pathway and then the pump pulse energy density was set to $1.6\,\mathrm{MJ\,kg^{-1}}$ using the first polarizer. One measurement was done for horizontal polarization and one measurement for vertical polarization. The polarization of the probe beam was unchanged between measurements.
The first method to compare the effects of both polarizations is the comparison of the created holes. Fig. 4.9a&b shows two holes in the same gold foil with an equal time delay between pump and probe pulse. The polarization of the pump beam is indicated by the arrows in the top left of each image. To help compare the hole shapes, the contours of the two holes are superimposed in Fig. 4.9c.
Both holes are asymmetric. They feature a spike on the right side, but are rounded at the top and bottom. However, the holes differ on the left hand side. The hole shot

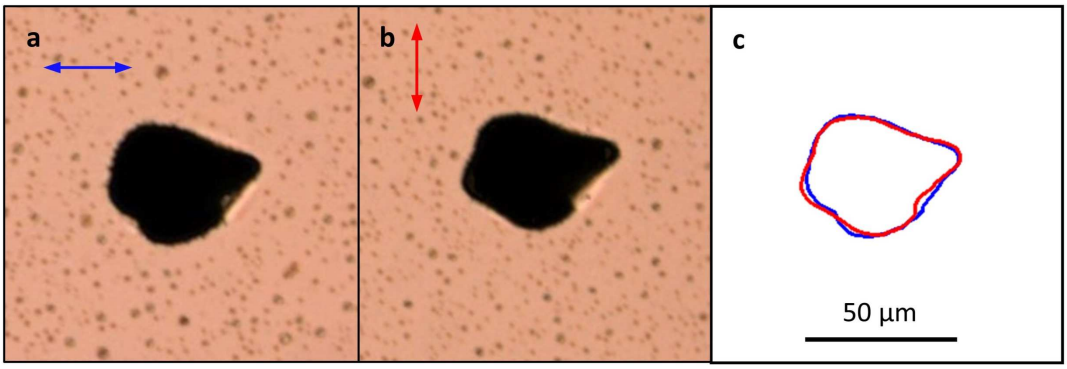

Figure 4.9.: a&b) Confocal microscope images of two holes in the gold foil with the polarization of the laser shown in the top left. Both holes were shot with a pump pulse energy density of $1.6\,\mathrm{MJ\,kg^{-1}}$ and at the same position of the delay stage of $75\,\mathrm{mm}$ which translates to a time delay of $91\,\mathrm{ps}$. **c)** Contour of the hole in a) (blue line) and b) (red line) superimposed.

with horizontal polarization is nearly round on the left side, whereas the hole shot with vertical polarization has a small spike on the left hand side.
Although some differences can be made up in the images, the contours of the holes are changed only slightly, similar to the variations observed when discussing the reproducibility of the measurements (see section 3.4). Furthermore, the changes are small compared to other studies that have observed significant elongation of the holes along the polarization axis [53, 54]. Therefore, the microscope images alone do not suggest a polarization dependence of the plasma dynamics.
Another method to check if the polarization of the pump beam influences the plasma dynamics, is the comparison of the *shot* images taken at the same time delays but with different pump polarization. If the plasma dynamics are independent of the polarization of the pump pulse, the images for a given time delay should be identical, regardless of the polarization.
A selection of three pairs of *shot* images with the same time delay for each pair, but different polarization of the pump pulse, is shown in Fig. 4.10. The pump pulse energy density for both polarizations was set to $1.6\,\mathrm{MJ\,kg^{-1}}$.
At a time delay of $0.68\,\mathrm{ps}$, the diffraction images for both polarizations look qualitatively similar. They have an intensity maxima in the center and some holographic features around it. There are no major differences in, for example, symmetry or width of the diffraction pattern that could indicate a polarization dependence.
At a time delay of $90\,\mathrm{ps}$, the diffraction images still show a similar structure. The central part of the image has a similar structure as the diffraction images at $0.68\,\mathrm{ps}$. In addition, a faint diffraction ring surrounds the central part. The ring is stretched vertically for both polarisations.
For a time delay of $990\,\mathrm{ps}$, both diffraction images again show a broadly similar structure. In the central part of the diffraction image the highest intensity of about 10^4 counts is observed. This maximum lies inside an area (see black dashed circle) that is near circular for the measurement with the vertical polarized pump pulse. In case of the horizontal pump polarization, the area surrounding the maximum is stretched vertically. The intensity decreases towards the edge of this area for both measurements where the intensity reaches a minimum.
Approximately $4\,\mathrm{mm}$ from the center, a ring is observed. Just like the ellipse in the center, this ring is elongated vertically for the measurement with horizontal polarization while it is about circular for the vertical polarized pump pulse. Furthermore, the ring does not have the same intensity for all diffraction angles. This is observed for both polarizations of the pump beam, but it is more eminent for the measurement with

vertical polarization. For the vertical polarization, one can make out four intensity maxima (see red arrows) and four minima.
In summary, the general structure of the diffraction images at different time delays is independent of the polarization of the pump beam. However, some differences in the diffraction images were observed, especially for the time delay of $990\,\mathrm{ps}$. This observation could indicate a polarization dependence of the plasma dynamics. However, to further discuss the influence of polarization on plasma dynamics, it will be important to compare the reconstructed complex transmissions for different polarizations at different time delays in the future.
Nevertheless, for both discussed methods the dependence of the plasma dynamics on the polarization is rather small when compared to other studies where laser pulses with similar pulse length were used [53, 54]. Therefore, further measurements for

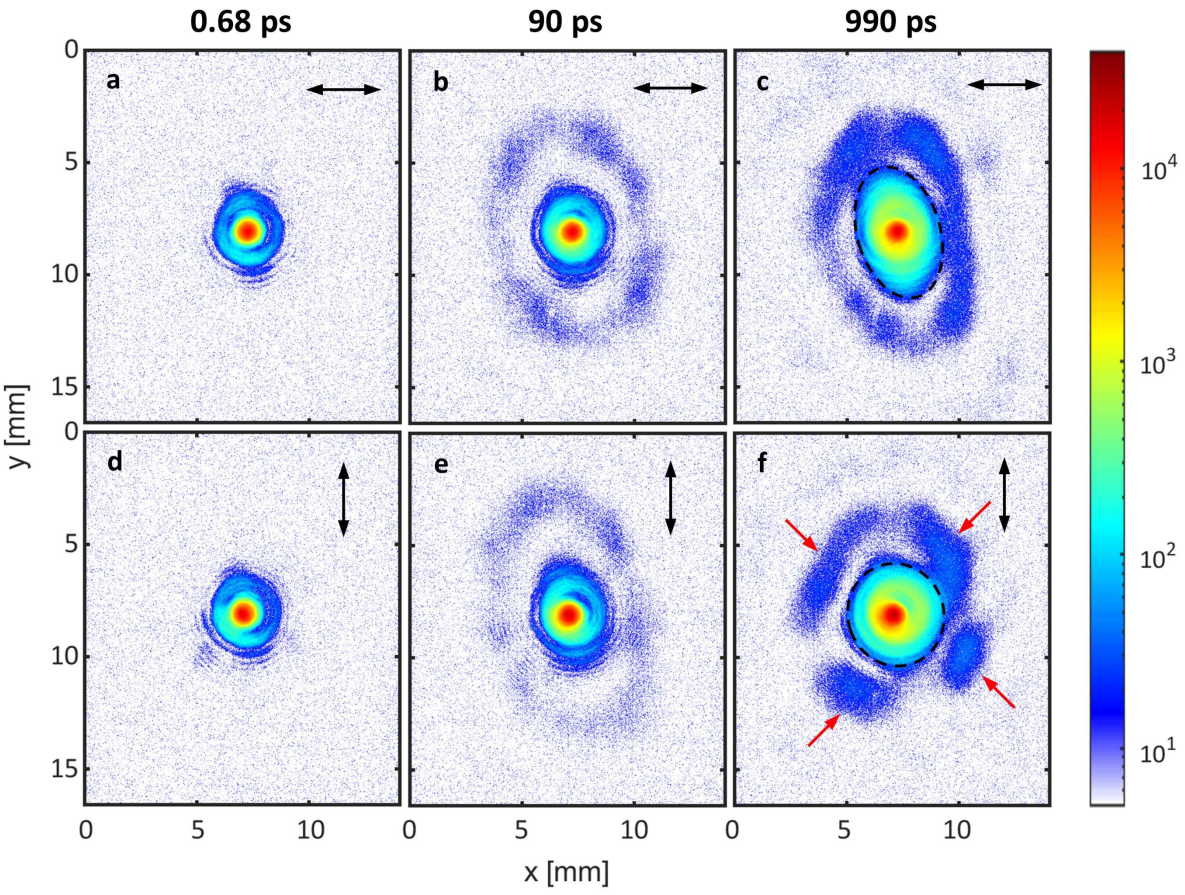

Figure 4.10.: *Shot*-diffraction images taken at three different time delays and two polarizations. The time delays are $0.68\,\mathrm{ps}$ (a,d), $90\,\mathrm{ps}$ (b,e) and $990\,\mathrm{ps}$ (c,f). The polarization direction is indicated by the arrow in the top right of each image. The pump energy density was set to $1.6\,\mathrm{MJ\,kg^{-1}}$ for all measurements.

different polarizations, including other orientations of linear polarization, circular and elliptic polarization, have to be carried out to prove or disprove a polarization dependence of the plasma dynamics in the case of thin free standing gold foils.

4.2. Reconstructions of the Spatially Resolved Transmission at the Target Position

The last sections were dedicated to the analysis of the captured diffraction images. However, the key technique in coherent diffractive imaging is the reconstruction of the electric field at the target position from the captured diffraction image using a phase retrieval algorithm. With the reconstructed electric field and the background field that was estimated from the *pre* measurement, the spatially resolved complex transmission, which includes the normalized transmission and phase shift with respect to the undisturbed foil, is calculated. It should be noted, that the calculated transmission in this section is the transmission of the electric field and not of the intensity, as it was the case in the prior sections.
The phase retrieval algorithm used for the reconstruction in thesis was developed by R. Altenkirch and C. Peltz at the Institute of Physics, University of Rostock in the group of Prof. Fennel: Strong-Field Nanophysics. A detailed explanation of the phase retrieval algorithm is given in the master's thesis of R. Altenkirch [43].
In this section, reconstructions of the complex transmission at the target position for *shot* images are presented. Since some reconstructions were unsuccessful, it is first discussed what criteria can be used to separate successful from failed reconstructions. Then, the plasma dynamics in the excited gold foil are discussed using the reconstructed complex transmission.

4.2.1. Criteria for Detecting Reconstruction Failures in Coherent Diffractive Imaging

As mentioned in the introduction of this section, not all diffraction images were reconstructed successfully. The criteria that are used to identify failed reconstructions are presented here.
One criterion for determining the success of a reconstruction is to check if the reconstructed complex transmission is physically reasonable. Examples for physically unreasonable transmissions include a change in transmission in an area that is significantly

larger than the pump beam and hole size. This would indicate that the transmission is altered in a region where the foil was undisturbed.
Additionally, the phase and amplitude of a realistic transmission map should show a smooth transition at the boundary between the excited and undisturbed regions. This is because the intensity profile of the pump beam and, therefore, the excitation of the foil, is continuous and not abrupt across its lateral direction. As a result, the refractive index of the foil is expected to exhibit a gradual change, leading to a smooth transition from the excited area to the non-excited foil in the reconstructed transmission. If instead a sharp or step-like change in transmission or phase is observed at the edge of the excited region, this indicates that the reconstruction has likely been unsuccessful.

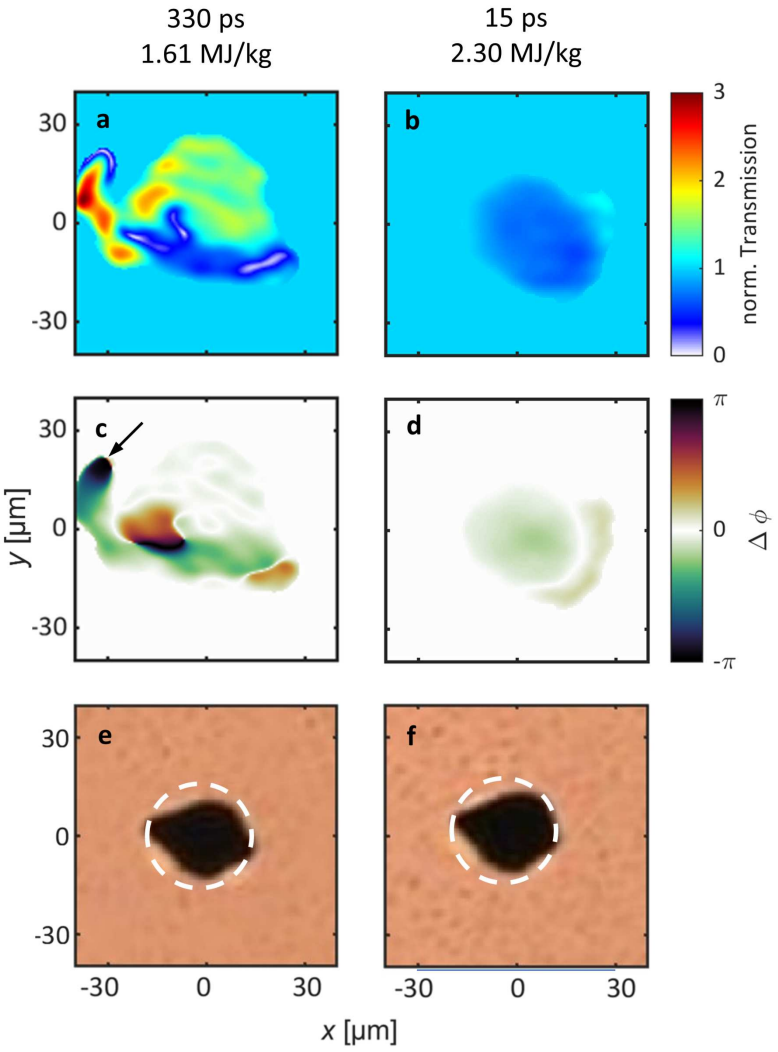

Figure 4.11.: Two reconstructions that failed. **top)** the reconstructed change in transmission, **middle)** the reconstructed change in phase and **bottom)** microscope images of the resulting holes and the $1/e^2$ pump beam size (white dashed circle).

Finally, if a transmission is observed that is higher than the transmission without a target, it would also be non-physical.
One reconstruction that falls into this first category is shown on the left side in Fig. 4.11. The normalized transmission (a) differs from 1 in an area that is significantly larger than the pump beam and hole size. Furthermore, the general shape of the reconstructed excited region differs greatly from the shape and size of the hole and pump beam and no symmetry is observable.
In addition, the phase (see Fig. 4.11c) of the electric field does not transition in a smooth manner from the excited to the undisturbed region. For example, the phase has a step like change from a phase shift of about $-\pi$ at the edge of the excited region to 0, the value in the undisturbed foil (see arrow).
In conclusion, the reconstruction shown on the left side in Fig. 4.11 and reconstructions showing similar features are physically unreasonable and as a result deemed unsuccessful.
Another point of failure in phase retrieval is the so called twin-image problem [55]. This is a typical phase retrieval problem that appears when objects that are nearly centrosymmetric are reconstructed. Instead of reconstructing the real image, a twin image is reconstructed. A twin image looks just like the real image, is but rotated by $180°$. Furthermore, the reconstructed phase values differ. The phase of the twin image is the inverse of the phase of the real image, i.e. the real images phase multiplied by -1. When the electric field of the twin image is propagated to the far field it produces a diffraction image identical to the diffraction image of the real image. Whether the real image or the twin image is reconstructed depends mainly on the random initial guess in the phase retrieval process. Furthermore, the probability that the twin image is reconstructed is increased when the target is placed in or near the focus of the probe beam and reduced if it is placed further away from the focus.
The right side in Fig. 4.11 shows a reconstruction that most likely falls into the twin image category. At a time delay of $15\,\mathrm{ps}$, a positive phase shift is expected, since the Drude model predicts an increase of the real part of the refractive index when the electron density is increased due excitation by the pump beam. However, a negative phase shift is reconstructed. For that reason, we can identify the reconstruction has failed most likely due to the twin-image problem. If one is able to correctly identify twin images, the real image could be obtained by inverting the phase and rotating the image by 180°.
While the twin image problem can be identified for measurements where one expects a certain phase shift, as it is the case in the first few picoseconds after excitation, it

can be difficult to identify this problem for other time delays where no expected phase is known. To identify twin images at later time delays, one can start by examining reconstructions at a point where the phase shift is already known, such as within the first few picoseconds after excitation. Since the phase shift is expected to evolve continuously over time, each reconstruction at a specific time delay can be compared to the previous one, where the real image is known. If a phase that is approximately the inverse of the previous image is observed, the reconstruction is most likely a twin image.
There exist some techniques to eliminate the twin image [55, 56, 57] such as the reduced-area support constraint method. Nonetheless, as the implementation of the phase retrieval algorithm is not part of this thesis, these techniques will not be discussed here.

4.2.2. Resolving Plasma Dynamics with Coherent Diffractive Imaging

In this section, the plasma dynamics in a $30\,\mathrm{nm}$ gold foil are discussed using successful reconstructions of the complex transmission at the target position. Fig. 4.12 shows the normalized reconstructed transmission (a-c) and the phase shift (d-f) with respect to the undisturbed foil for three *shot* measurements. In addition, microscope images of the corresponding holes are shown (g-i). The three different time delays are $35\,\mathrm{ps}$, $245\,\mathrm{ps}$ and $793\,\mathrm{ps}$ and the absorbed energy density is $1.61\,\mathrm{MJ\,kg^{-1}}$ for all three given time delays. Both the reconstructed transmissions and phases deviate from the undisturbed foil in an area that is similar in size and shape to the hole in the gold foil after the measurement. The reconstructions and the holes are elongated in $x-$direction. This further indicates, that the reconstructions shown in Fig. 4.12 were successful.
The normalized transmission at $35\,\mathrm{ps}$ is reduced in the excited area when compared to the undisturbed foil (see Fig. 4.12a). This fits well with the earlier observation (section 4.1.1), where the time resolved transmission was discussed and a reduced transmission with respect to the undisturbed foil was found at a time delay of $35\,\mathrm{ps}$.
In addition, the normalized transmission is not homogeneous, but features some structure. For example, the transmission is slightly reduced in the central part of the excited area (see arrow A), is then increased slightly in the surrounding area (see arrow B), indicated by a lighter blue tone, before being decreased again at the edge of the excited area (see arrow C). This structure could indicate ongoing lattice dynamics, since an exclusive excitation of electrons should change the refractive index and the transmission

similar to the pump beam profile, which is nearly Gaussian. The ring-like structure is not very pronounced when compared to other reconstructions at later time delays (see Fig. 4.12b&c).

The phase shift at $35\,\mathrm{ps}$ is positive in the excited region (see Fig. 4.12d). Notably, the phase shift is largest in the central part (see arrow A), where a local minimum in the normalized transmission was observed. A positive phase shift implies a longer optical

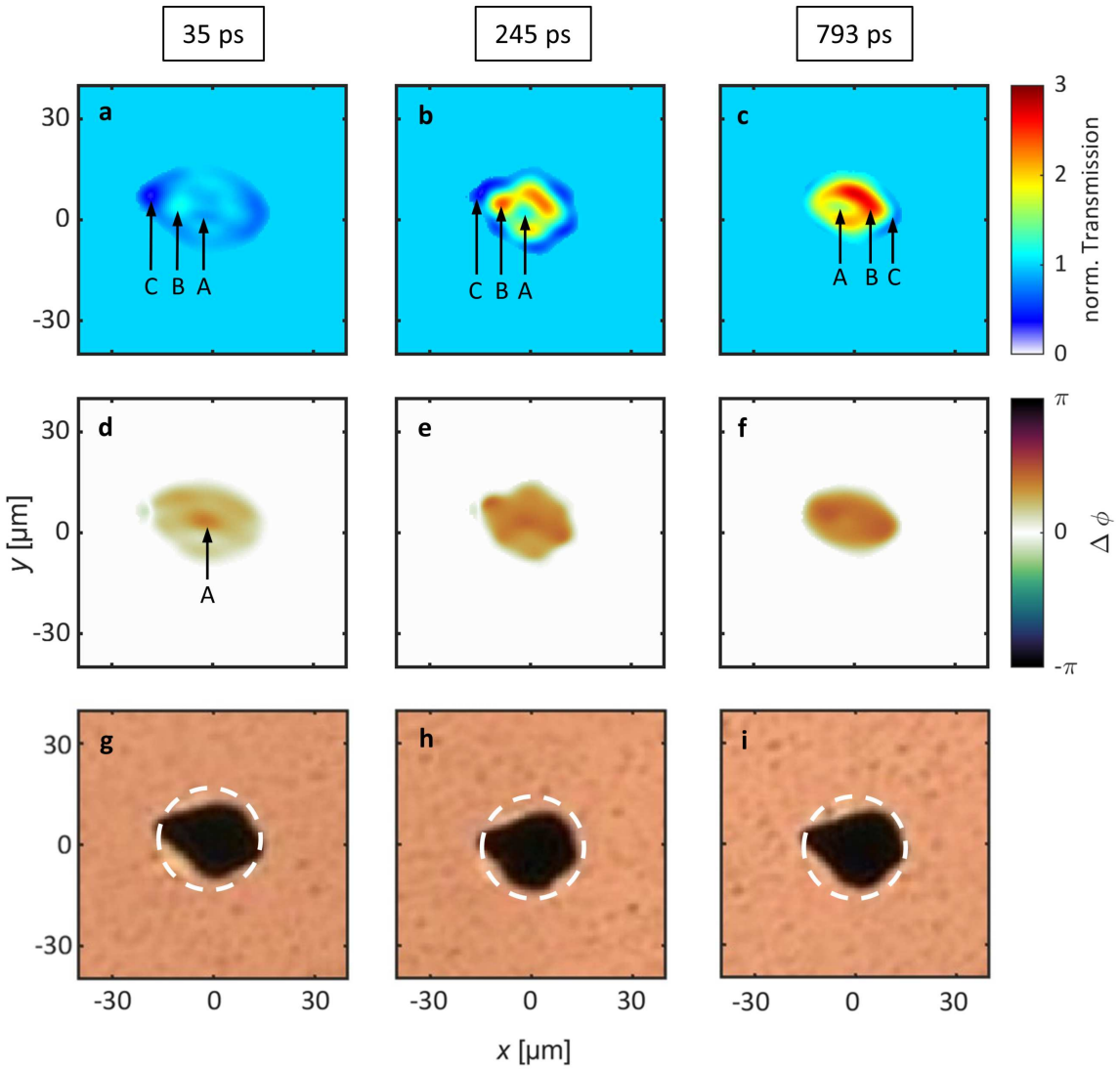

Figure 4.12.: Comparison of reconstructions of the complex transmission: The normalized transmission (**top**) and the phase shift (**middle**) with respect to the undisturbed foil for three shot measurements are shown. In addition, microscope images of the corresponding holes and the $1/e^2$ pump beam size (white dashed circle) are shown (**bottom**). The time delays are **left)** $35\,\mathrm{ps}$, **middle)** $245\,\mathrm{ps}$ and **right)** $793\,\mathrm{ps}$. The absorbed energy density for all measurements was $1.61\,\mathrm{MJ\,kg^{-1}}$.

pathway, which indicates an increase in the real part of the refractive index in this region.
In the Drude model, an increase in the real part of the refractive index is observed when the plasma frequency is increased. Since the plasma frequency increases with a rise in the free electron density, the positive phase shift is most likely due to the excitation of electrons. This increases the free electron density in the foil and results in a positive phase shift. The increased phase shift in the center can be explained by reasoning, that the excitation in the central region is stronger, since a Gaussian laser pulse is most intense in the center.
$245\,\mathrm{ps}$ after the pump laser excitation, the transmission in the center of the excited region has increased to nearly one (see arrow A in Fig. 4.12b). Surrounding the center, a ring-like shape with increased transmission in the range of 1.3 to 2 is observed (see arrow B). This ring is surrounded by another ring-like shape with transmission values smaller than 1 (see arrow C) .
Since the transmission is above one in most parts of the excited area, the reconstruction fits the earlier analysis where the total transmission was observed to exceed 1 after $100\,\mathrm{ps}$ (see section 4.1.1). The ongoing lattice dynamics possibly lead to a increased thickness of the plasma, reducing the free electron density. As a consequence, this reduces the reflection and an increased transmission is observed.
The distinct structure of the reconstructed transmission could be due to the lattice dynamics in the foil that ultimately lead to an expansion of the plasma and, therefore, to the formation of a three dimensional object, known as a plasma plume [58]. As the light is diffracted on this 3D object, but the electric field is reconstructed on a two dimensional plane, the reconstruction essentially maps the 3D object onto a 2D plane. Retrieving the full three-dimensional structure of the plasma, including the spatially resolved refractive index, is challenging and only possible with some assumptions about the object.
Nevertheless, ring-like features have been observed in other studies regarding laser ablation. When the reflected probe light was used to image the ablation dynamics, Newton rings where observed at similar time delays of some hundreds of picoseconds for metals, semiconductors and dielectrics [59, 60, 61]. The observation of Newton rings was assigned to the spallation of a thin liquid layer from the target. The observation of ring-like features could indicate a similar behavior for thin gold foils.
The phase shift seen in Fig. 4.12e at a time delay of $245\,\mathrm{ps}$ is positive. This implies a longer optical pathway. This could be due to an increased refractive index in this region due to the excitation of electrons as discussed above, or due to a larger prop-

agation distance in the medium, as the plasma is expanding. However, opposing to the phase shift for a time delay of $35\,\mathrm{ps}$, the phase shift is mostly homogeneous over the extend of the excited region. Nevertheless, the interpretation of the spatial phase distribution is challenging, as the probe light was most likely diffracted at a three dimensional object. Therefore, a detailed interpretation of the phase shift is left to the future.

At a time delay of $793\,\mathrm{ps}$, the transmission in the center of the excited area is increased when compared to $245\,\mathrm{ps}$ (see 4.12c). The general structure is similar to the structure observed at a time delay of $245\,\mathrm{ps}$. The increased transmission fits the earlier analysis, where an increase in transmission with prolonged time delay was observed (see section 4.1.1). In the central part, the transmission reaches values of about 1.7 (see arrow A). It is surrounded by a ring-like shape with increased transmission in the range of 1.9 to 2.7 (see arrow B). The transmission is highest in the upper right part of the ring and lowest in the lower left part. This ring is surrounded by another ring-like shape with decreased transmission (see arrow C). This observation could be due to the same effects discussed for the time delay of $245\,\mathrm{ps}$, namely that the three dimensional plasma is imaged with the probe pulse at a two dimensional plane which could lead to ring-like structures such as Newton rings and indicate the spallation of liquid layers.

The phase shift is again positive and homogeneous in the excited area. As before, a detailed interpretation of the phase shift is left to the future.

In conclusion, the reconstruction of the complex transmission was successful for multiple time delays ranging from some ten to hundreds of picoseconds. For the presented successful reconstructions, a ring-like structure overlaying the normalized transmission was observed. The appearance of the structures where attributed to the lattice dynamics in the excited gold foil and to a possible spallation of liquid layers. All results of the reconstructions are in agreement with the results discussed in section 4.1.1 and 4.1.2.

Possible future improvements include the development of a method to reconstruct the 3D spatially resolved refractive index of the generated plasma from the 2D complex transmission. In addition, a detailed analysis of which experimental parameters lead to successful reconstructions may lead to a higher reliability of the phase retrieval algorithm. Furthermore, theoretical studies of the plasma dynamics can help to interpret the data, especially the phase distribution, in more detail.

Chapter 5.

Conclusion and Outlook

The goal of this thesis has been to investigate the plasma dynamics in thin 30 nm gold foils after excitation by an 800 nm femtosecond pump pulse. The dynamics are imaged by means of coherent diffractive imaging with a 400 nm probe pulse that is diffracted by the excited gold foil. The diffraction image taken with a detector in the far-field provides information about the dynamics in the excited gold foil.
One important part of the thesis has been the improvement of the stability of the setup. It has been demonstrated that the reproducibility of measurements can be enhanced by implementing a beam stabilization system and a well-designed optical mounting configuration. The high stability was verified by comparing holes in the gold foil at different time delays, as well as diffraction images taken with unchanged experimental parameters and only insignificant changes were found. Furthermore, the influence of the pump pulse energy and polarization on the plasma dynamics was discussed. It was found that the decrease in transmission in the first 10 ps after excitation by the pump beam is due to the excitation of the electrons in the gold foil. After about 15 ps, the energy transfer from the electrons to the lattice leads to the melting of the excited foil and finally to an expansion of the induced plasma. With increasing pump energy, an increase in the free electron density and larger ablation areas were observed. In addition, the ablation threshold for thin gold foils, which is in agreement with other studies, was determined. When changing the polarization of the pump beam, small differences in the dynamics were observed. The variations in the shapes of the holes are similar to the changes observed in the analysis of the stability of the setup. To make statements about a dependence of the dynamics on the pump polarization, further measurements are required.
With the time-resolved diffraction images of a laser excited 30 nm thick gold foil recorded during this thesis, it was possible to successfully reconstruct the spatially and time-resolved complex transmission of the foil for multiple time delays using a

phase retrieval algorithm developed by R. Altenkirch and C. Peltz. By analyzing the reconstructed complex transmissions, information about the plasma dynamics within the foil was obtained. A ring-like structure in the transmission map was observed for time delays between 35 ps to 800 ps and attributed to the lattice dynamics in the foil. Additionally, as still some reconstruction attempts failed, criteria to identify unsuccessful reconstructions of the complex transmission were presented.

Some possible future improvements to the setup were identified. Since the dynamics in the gold foil are not finished after the maximum time delay of 2 ns, a longer maximum time delay would allow for imaging of the dynamics at later times. This could be achieved by passing the delay stage a second time. In addition, a detailed analysis of which experimental parameters lead to successful reconstructions may lead to a higher reliability of the phase retrieval algorithm.

In conclusion, during this thesis a successful experimental setup for the investigation of plasma dynamics in thin gold foils using coherent diffractive imaging was presented. With the setup, it was possible to obtain information about the plasma dynamics in thin gold foils from the captured diffraction images as well as from the reconstructed complex time- and spatially-resolved transmission. As the experimental method has proven successful for thin gold foils, the response of other targets, such as semiconductors and insulators, to excitation by ultrashort laser pulses can be studied using this setup in the future.

Appendix A.

Attachments

A.1. Calculation of the Transmitted and Reflected Electric Fields for Thin Films

To calculate the total transmitted and reflected electric fields for a thin film one has to add up all contributions of the electric field that are reflected and transmitted, respectively.
For the transmission this is:

$$
\begin{aligned}
E_T =& E_{T1} + E_{T2} + E_{T3} + \dots && \text{(A.1)}\\
=& E_0 \cdot t_1 t_2 e^{-\alpha L} e^{\mathrm{i}kL} && \text{(A.2)}\\
&+ E_0 \cdot t_1 t_2 r^2 e^{-3\alpha L} e^{3\mathrm{i}kL} && \text{(A.3)}\\
&+ E_0 \cdot t_1 t_2 r^4 e^{-5\alpha L} e^{5\mathrm{i}kL} && \text{(A.4)}\\
&+ \dots && \text{(A.5)}\\
=& E_0 \cdot t_1 t_2 e^{-\alpha L} e^{\mathrm{i}kL} (1 + r^2 e^{-2\alpha L} e^{2ikL} + r^4 e^{-4\alpha L} e^{4\mathrm{i}kL} + \dots) && \text{(A.6)}\\
=& E_0 \cdot t_1 t_2 e^{-\alpha L} e^{\mathrm{i}kL} \sum_{n=0}^{\infty} r^{2n} e^{-2n\alpha L} e^{2n\mathrm{i}kL} && \text{(A.7)}\\
=& E_0 \cdot t_1 t_2 e^{-\alpha L} e^{\mathrm{i}kL} \sum_{n=0}^{\infty} \left(r^n e^{-n\alpha L} e^{n\mathrm{i}kL} \right)^2 && \text{(A.8)}\\
=& E_0 t_1 t_2 e^{\mathrm{i}kL} e^{-\alpha L} \frac{1}{1 - \left(r \cdot e^{-\alpha L} e^{\mathrm{i}kL} \right)^2} && \text{(A.9)}
\end{aligned}
$$

In the last step, the definition of a geometric series $\sum_{n=0}^{\infty} q^n = \frac{1}{1-q}$ for $|q| < 1$ is used. The condition is fulfilled as $|r| \leq 1$, $|e^{-\alpha L}| < 1$ for $L > 0$, $\alpha > 0$ and $|e^{\mathrm{i}kL}| = 1$ for all L and k.

The appearance of the terms can be explained intuitively, when transmission and reflection and the absorption and phase shift in the medium are taken care of. The first contribution E_{R1} is the part of incoming electric field E_0 transmitted through the air-gold interface (t_1), absorbed over the thickness L of the foil ($e^{-\alpha L}$) with a phase shift ($e^{\mathrm{i}kL}$) and the transmission through the second interface gold to air (t_2).
For the following contributions, the beam passes the thickness of the foil two more times than the contribution before, resulting in further absorption ($e^{-2\alpha L}$) and phase shift ($e^{2\mathrm{i}kL}$) over two times the foil thickness and reflections at the two interfaces of the foil (r^2).
A similar approach is used to calculate the reflected electric field:

$$
\begin{aligned}
E_R =& E_{R1} + E_{R2} + E_{R3} + \dots && \text{(A.10)}\\
=& E_0 \cdot r && \text{(A.11)}\\
&+ E_0 \cdot r t_1 t_2 e^{2\mathrm{i}kL} e^{-2\alpha L} && \text{(A.12)}\\
&+ E_0 \cdot r^3 t_1 t_2 e^{4\mathrm{i}kL} e^{-4\alpha L} && \text{(A.13)}\\
&+ \dots && \text{(A.14)}\\
=& E_0 r \left(1 + t_1 t_2 e^{2\mathrm{i}kL} e^{-2\alpha L} \left(+ r^2 e^{2\mathrm{i}kL} e^{-2\alpha L} \dots\right)\right) && \text{(A.15)}\\
=& E_0 r \left(1 + t_1 t_2 e^{2\mathrm{i}kL} e^{-2\alpha L} \sum_{n=0}^{\infty} (r e^{\mathrm{i}kL} e^{-\alpha L})^2\right) && \text{(A.16)}\\
=& E_0 r \left(1 + t_1 t_2 e^{2\mathrm{i}kL} e^{-2\alpha L} \frac{1}{1 - (r e^{\mathrm{i}kL} e^{-\alpha L})^2}\right) && \text{(A.17)}
\end{aligned}
$$

In the last step, the definition of a geometric series $\sum_{n=0}^{\infty} q^n = \frac{1}{1-q}$ for $|q| < 1$ is used. The condition is fulfilled as $|r| \leq 1$, $|e^{-\alpha L}| < 1$ for $L > 0$, $\alpha > 0$ and $|e^{\mathrm{i}kL}| = 1$ for all L and k.
The appearance of the terms can again be explained intuitively, when transmission and reflection and the absorption and phase shift in the medium are taken care of. The first contribution E_{T1} is the part of incoming electric field E_0 that is reflected (r) at the air-gold interface.
For the following contributions, the beam is transmitted through the gold-air interface (t_1), reflected at the backside of the foil (r) and transmitted at the foil-air interface (t_2). Furthermore, it passes the thickness of the foil two times, resulting in a phase shift ($e^{2\mathrm{i}kL}$) and absorption ($e^{-2\alpha L}$). All further contributions pass the thickness of the foil two more times than the contribution before, resulting in further absorption ($e^{-2\alpha L}$) and phase shift (e^{2ikL}) over two times the foil thickness. Additionally, the beam is reflected at the two interfaces of the foil (r^2).

To conclude the total reflected (E_R) and transmitted (E_T) electric field for a thin film is given by:

$$E_R = E_0 \cdot t_1 t_2 e^{\mathrm{i}kL} e^{-\alpha L} \frac{1}{1 - (r e^{-\alpha L} e^{\mathrm{i}kL})^2} \tag{A.18}$$

$$E_T = E_0 r \left(1 + t_1 t_2 e^{2\mathrm{i}kL} e^{-2\alpha L} \frac{1}{1 - (r e^{\mathrm{i}kL} e^{-\alpha L})^2} \right) \tag{A.19}$$

Bibliography

[1] PERRY, M. D. ; STUART, B. C. ; BANKS, P. S. ; FEIT, M. D. ; YANOVSKY, V. ; RUBENCHIK, A. M.: Ultrashort-pulse laser machining of dielectric materials. In: *Journal of Applied Physics* 85 (1999), 05, Nr. 9, 6803-6810. http://dx.doi.org/10.1063/1.370197. – DOI 10.1063/1.370197. – ISSN 0021–8979

[2] PECHOLT, B. ; VENDAN, M. ; DONG, Y. ; MOLIAN, P. : Ultrafast laser micromachining of 3C-SiC thin films for MEMS device fabrication. In: *International Journal of Advanced Manufacturing Technology* 39 (2008), Nr. 3-4, S. 239–250. http://dx.doi.org/10.1007/s00170-007-1223-5. – DOI 10.1007/s00170–007–1223–5. – ISSN 02683768

[3] RETHFELD, B. ; IVANOV, D. S. ; GARCIA, M. E. ; ANISIMOV, S. I.: Modelling ultrafast laser ablation. In: *Journal of Physics D: Applied Physics* 50 (2017), Nr. 19. http://dx.doi.org/10.1088/1361-6463/50/19/193001. – DOI 10.1088/1361–6463/50/19/193001. – ISSN 13616463

[4] SIMON, P. ; IHLEMANN, J. : Machining of submicron structures on metals and semiconductors by ultrashort UV-laser pulses. In: *Applied Physics A: Materials Science and Processing* 63 (1996), Nr. 5, S. 505–508. http://dx.doi.org/10.1007/BF01571681. – DOI 10.1007/BF01571681. – ISSN 09478396

[5] ENGLERT, L. ; WOLLENHAUPT, M. ; HAAG, L. ; SARPE-TUDORAN, C. ; RETHFELD, B. ; BAUMERT, T. : Material processing of dielectrics with temporally asymmetric shaped femtosecond laser pulses on the nanometer scale. In: *Applied Physics A: Materials Science and Processing* 92 (2008), Nr. 4, S. 749–753. http://dx.doi.org/10.1007/s00339-008-4584-1. – DOI 10.1007/s00339–008–4584–1. – ISSN 09478396

[6] HWANG, D. J. ; GRIGOROPOULOS, C. P. ; CHOI, T. Y.: Efficiency of silicon micromachining by femtosecond laser pulses in ambient air. In: *Journal of Applied Physics* 99 (2006), 04, Nr. 8, 083101. http://dx.doi.org/10.1063/1.2187196. – DOI 10.1063/1.2187196. – ISSN 0021–8979

[7] CHENG, J. ; PERRIE, W. ; EDWARDSON, S. ; FEARON, E. ; DEARDEN, G. ; WATKINS, K. : Effects of laser operating parameters on metals micromachining with ultrafast lasers. In: *Applied Surface Science* 256 (2009), Nr. 5, 1514-1520. http://dx.doi.org/https://doi.org/10.1016/j.apsusc.2009.09.013. – DOI https://doi.org/10.1016/j.apsusc.2009.09.013. – ISSN 0169–4332. – Proceedings of the Symposium on Surface Science 2008 Festschrift in honor of Professor Şefik Süzer's 60th birthday

[8] CHAPMAN, H. N. ; NUGENT, K. A.: Coherent lensless X-ray imaging. In: *Nature Photonics* 4 (2010), Nr. 12, S. 833–839. http://dx.doi.org/10.1038/nphoton.2010.240. – DOI 10.1038/nphoton.2010.240. – ISSN 17494885

[9] FIENUP, J. R.: Phase retrieval algorithms: a comparison. In: *Applied Optics* 21 (1982), Nr. 15, S. 2758. http://dx.doi.org/10.1364/ao.21.002758. – DOI 10.1364/ao.21.002758. – ISSN 0003–6935

[10] ANISIMOV, S. ; KAPELIOVICH, B. ; PERELMAN, T. u. a.: Electron emission from metal surfaces exposed to ultrashort laser pulses. In: *Zh. Eksp. Teor. Fiz* 66 (1974), Nr. 2, S. 375–377

[11] BÖTTCHER, T. : *Zeitaufgelöste Holografie von dünnen Goldfolien*, University of Rostock, Bachelor Thesis, 2022

[12] MENDOZA HERRERA, L. J. ; ARBOLEDA, D. M. ; SCHINCA, D. C. ; SCAFFARDI, L. B.: Determination of plasma frequency, damping constant, and size distribution from the complex dielectric function of noble metal nanoparticles. In: *Journal of Applied Physics* 116 (2014), 12, Nr. 23, 233105. http://dx.doi.org/10.1063/1.4904349. – DOI 10.1063/1.4904349. – ISSN 0021–8979

[13] BABAR, S. ; WEAVER, J. H.: Optical constants of Cu, Ag, and Au revisited. In: *Appl. Opt.* 54 (2015), Jan, Nr. 3, 477–481. http://dx.doi.org/10.1364/AO.54.000477. – DOI 10.1364/AO.54.000477

[14] PYYKKO, P. ; DESCLAUX, J. P.: Relativity and the Periodic System of Elements. In: *Accounts of Chemical Research* 12 (1979), Nr. 8, S. 276–281. http://dx.doi.org/10.1021/ar50140a002. – DOI 10.1021/ar50140a002. – ISSN 15204898

[15] HECHT, E. : *Optik*. Walter de Gruyter GmbH & Co KG, 2023

[16] ZHAO, X. ; SHIN, Y. C.: A two-dimensional comprehensive hydrodynamic model for femtosecond laser pulse interaction with metals. In: *Journal of Physics D: Applied Physics* 45 (2012), Nr. 10. http://dx.doi.org/10.1088/0022-3727/45/10/105201. – DOI 10.1088/0022–3727/45/10/105201. – ISSN 00223727

[17] B.N. CHICBKOV, C. MOMMA, S. NOLTE, F. VON ALVENSLEBEN, A. T.: Femtosecond, picosecond and nanosecond laser ablation of solids. In: *Applied Physics A* 63 (1996), Nr. 1-2, S. 109–115. http://dx.doi.org/10.1007/BF01567637. – DOI 10.1007/BF01567637

[18] FUJIMOTO, J. G. ; LIU, J. M. ; IPPEN, E. P. ; BLOEMBERGEN, N. : Femtosecond Laser Interaction with Metallic Tungsten and Nonequilibrium Electron and Lattice Temperatures. In: *Phys. Rev. Lett.* 53 (1984), Nov, 1837–1840. http://dx.doi.org/10.1103/PhysRevLett.53.1837. – DOI 10.1103/PhysRevLett.53.1837

[19] HOHLFELD, J. ; WELLERSHOFF, S. S. ; GÜDDE, J. ; CONRAD, U. ; JÄHNKE, V. ; MATTHIAS, E. : Electron and lattice dynamics following optical excitation of metals. In: *Chemical Physics* 251 (2000), Nr. 1-3, S. 237–258. http://dx.doi.org/10.1016/S0301-0104(99)00330-4. – DOI 10.1016/S0301–0104(99)00330–4. – ISSN 03010104

[20] KARNA, P. ; HOQUE, M. S. B. ; THAKUR, S. ; HOPKINS, P. E. ; GIRI, A. : Direct Measurement of Ballistic and Diffusive Electron Transport in Gold. In: *Nano Letters* 23 (2023), Nr. 2, S. 491–496. http://dx.doi.org/10.1021/acs.nanolett.2c03781. – DOI 10.1021/acs.nanolett.2c03781. – ISSN 15306992

[21] KHVAN, A. ; USPENSKAYA, I. ; ARISTOVA, N. ; CHEN, Q. ; TRIMARCHI, G. ; KONSTANTINOVA, N. ; DINSDALE, A. : Description of the thermodynamic properties of pure gold in the solid and liquid states from 0 K. In: *Calphad* 68 (2020), 101724. http://dx.doi.org/https://doi.org/10.1016/j.calphad.2019.101724. – DOI https://doi.org/10.1016/j.calphad.2019.101724. – ISSN 0364–5916

[22] WILDE, G. ; MITSCH, C. ; GÖRLER, G. ; WILLNECKER, R. : Specific heat and related thermodynamic functions of undercooled Cu-Ni and Au melts. In: *Journal of Non-Crystalline Solids* 205-207 (1996), 425-429. http://dx.doi.org/https://doi.org/10.1016/S0022-3093(96)00451-6. – DOI https://doi.org/10.1016/S0022–3093(96)00451–6. – ISSN 0022–3093. – Ninth International Conference on Liquid and Amorphous Metals

[23] *WebElements*. https://www.webelements.com, Last checked: April 2024

[24] BYSKOV-NIELSEN, J. ; SAVOLAINEN, J. M. ; CHRISTENSEN, M. S. ; BALLING, P. : Ultra-short pulse laser ablation of copper, silver and tungsten: Experimental data and two-temperature model simulations. In: *Applied Physics A: Materials Science and Processing* 103 (2011), Nr. 2, S. 447–453. http://dx.doi.org/10.1007/s00339-011-6363-7. – DOI 10.1007/s00339–011–6363–7. – ISBN 0033901163

[25] HODAK, J. H. ; HENGLEIN, A. ; HARTLAND, G. V.: Electron-phonon coupling dynamics in very small (between 2 and 8 nm diameter) Au nanoparticles. In: *Journal of Chemical Physics* 112 (2000), Nr. 13, S. 5942–5947. http://dx.doi.org/10.1063/1.481167. – DOI 10.1063/1.481167. – ISSN 00219606

[26] WANG, W. ; CAHILL, D. G.: Limits to thermal transport in nanoscale metal bilayers due to weak electron-phonon coupling in Au and Cu. In: *Physical Review Letters* 109 (2012), Nr. 17, S. 1–5. http://dx.doi.org/10.1103/PhysRevLett.109.175503. – DOI 10.1103/PhysRevLett.109.175503. – ISSN 00319007

[27] HOSTETLER, J. L. ; SMITH, A. N. ; CZAJKOWSKY, D. M. ; NORRIS, P. M.: Measurement of the electron-phonon coupling factor dependence on film thickness and grain size in Au, Cr, and Al. In: *Applied Optics* 38 (1999), Nr. 16, S. 3614. http://dx.doi.org/10.1364/ao.38.003614. – DOI 10.1364/ao.38.003614. – ISSN 0003–6935

[28] JAIN, A. ; MCGAUGHEY, A. J.: Thermal transport by phonons and electrons in aluminum, silver, and gold from first principles. In: *Physical Review B* 93 (2016), Nr. 8, S. 1–5. http://dx.doi.org/10.1103/PhysRevB.93.081206. – DOI 10.1103/PhysRevB.93.081206. – ISSN 24699969

[29] MUELLER, B. Y. ; RETHFELD, B. : Nonequilibrium electron-phonon coupling after ultrashort laser excitation of gold. In: *Applied Surface Science* 302 (2014), 24–28. http://dx.doi.org/10.1016/j.apsusc.2013.12.074. – DOI 10.1016/j.apsusc.2013.12.074. – ISSN 01694332

[30] IVANOV, D. ; ZHIGILEI, L. : Combined atomistic-continuum modeling of short-pulse laser melting and disintegration of metal films. In: *Physical Review B - Condensed Matter and Materials Physics* 68 (2003), Nr. 6, S. 1–22. http://dx.doi.org/10.1103/PhysRevB.68.064114. – DOI 10.1103/PhysRevB.68.064114. – ISSN 1550235X

[31] MO, M. Z. ; CHEN, Z. ; LI, R. K. ; DUNNING, M. ; WITTE, B. B. ; BALDWIN, J. K. ; FLETCHER, L. B. ; KIM, J. B. ; NG, A. ; REDMER, R. ; REID, A. H. ; SHEKHAR, P. ; SHEN, X. Z. ; SHEN, M. ; SOKOLOWSKI-TINTEN, K. ; TSUI, Y. Y. ; WANG, Y. Q. ; ZHENG, Q. ; WANG, X. J. ; GLENZER, S. H.: Heterogeneous to homogeneous melting transition visualized with ultrafast electron diffraction. In: *Science* 360 (2018), Nr. 6396, S. 1451–1455. http://dx.doi.org/10.1126/science.aar2058. – DOI 10.1126/science.aar2058. – ISSN 10959203

[32] SOKOLOWSKI-TINTEN, K. ; BIALKOWSKI, J. ; BOING, M. ; CAVALLERI, A. : Thermal and nonthermal melting of gallium arsenide after femtosecond laser excitation. In: *Physical Review B - Condensed Matter and Materials Physics* 58 (1998), Nr. 18, S. R11805–R11808. http://dx.doi.org/10.1103/PhysRevB.58.R11805. – DOI 10.1103/PhysRevB.58.R11805. – ISSN 1550235X

[33] CHAN, W. L. ; AVERBACK, R. S. ; CAHILL, D. G. ; LAGOUTCHEV, A. : Dynamics of femtosecond laser-induced melting of silver. In: *Physical Review B - Condensed Matter and Materials Physics* 78 (2008), Nr. 21, S. 1–8. http://dx.doi.org/10.1103/PhysRevB.78.214107. – DOI 10.1103/PhysRevB.78.214107. – ISSN 10980121

[34] AREFEV, M. I. ; SHUGAEV, M. V. ; ZHIGILEI, L. V.: Kinetics of laser-induced melting of thin gold film: How slow can it get? In: *Science Advances* 8 (2022), Nr. 38, S. 1–16. http://dx.doi.org/10.1126/sciadv.abo2621. – DOI 10.1126/sciadv.abo2621. – ISSN 23752548

[35] WU, C. ; ZHIGILEI, L. V.: Microscopic mechanisms of laser spallation and ablation of metal targets from large-scale molecular dynamics simulations. In: *Applied Physics A: Materials Science and Processing* 114 (2014), jan, Nr. 1, S. 11–32. http://dx.doi.org/10.1007/s00339-013-8086-4. – DOI 10.1007/s00339–013–8086–4. – ISSN 09478396

[36] YATSUHASHI, T. ; NAKASHIMA, N. : Multiple ionization and Coulomb explosion of molecules, molecular complexes, clusters and solid surfaces. In: *Journal of Photochemistry and Photobiology C: Photochemistry Reviews* 34 (2018), 52-84. http://dx.doi.org/https://doi.org/10.1016/j.jphotochemrev.2017.12.001. – DOI https://doi.org/10.1016/j.jphotochemrev.2017.12.001. – ISSN 1389–5567

[37] LI, S. ; LI, S. ; ZHANG, F. ; TIAN, D. ; LI, H. ; LIU, D. ; JIANG, Y. ; CHEN, A. ; JIN, M. : Possible evidence of Coulomb explosion in the femtosecond laser ablation of metal at low laser fluence. In: *Applied Surface Science* 355 (2015), 681-685. http://dx.doi.org/https://doi.org/10.1016/j.apsusc.2015.07.136. – DOI https://doi.org/10.1016/j.apsusc.2015.07.136. – ISSN 0169–4332

[38] WU, C. ; ZHIGILEI, L. V.: Microscopic mechanisms of laser spallation and ablation of metal targets from large-scale molecular dynamics simulations. In: *Applied Physics A: Materials Science and Processing* 114 (2014), Nr. 1, S. 11–32. http://dx.doi.org/10.1007/s00339-013-8086-4. – DOI 10.1007/s00339–013–8086–4. – ISSN 09478396

[39] TSKHAKAYA, D. ; MATYASH, K. ; SCHNEIDER, R. ; TACCOGNA, F. : The Particle-In-Cell Method. In: *Contributions to Plasma Physics* 47 (2007), Nr. 8-9, 563-594. http://dx.doi.org/https://doi.org/10.1002/ctpp.200710072. – DOI https://doi.org/10.1002/ctpp.200710072

[40] ESIRKEPOV, T. ; BORGHESI, M. ; BULANOV, S. V. ; MOUROU, G. ; TAJIMA, T. : Highly efficient relativistic-ion generation in the laser-piston regime. In: *Physical Review Letters* 92 (2004), Nr. 17, S. 2–5. http://dx.doi.org/10.1103/PhysRevLett.92.175003. – DOI 10.1103/PhysRevLett.92.175003. – ISSN 00319007

[41] KAR, S. ; BORGHESI, M. ; BULANOV, S. V. ; KEY, M. H. ; LISEYKINA, T. V. ; MACCHI, A. ; MACKINNON, A. J. ; PATEL, P. K. ; ROMAGNANI, L. ; SCHIAVI, A. ; WILLI, O. : Plasma jets driven by ultraintense-laser interaction with thin foils. In: *Physical Review Letters* 100 (2008), Nr. 22, S. 1–4. http://dx.doi.org/10.1103/PhysRevLett.100.225004. – DOI 10.1103/PhysRevLett.100.225004. – ISSN 00319007

[42] KING, M. ; GRAY, R. J. ; POWELL, H. W. ; MACLELLAN, D. A. ; GONZALEZ-IZQUIERDO, B. ; STOCKHAUSEN, L. C. ; HICKS, G. S. ; DOVER, N. P. ; RUSBY, D. R. ; CARROLL, D. C. ; PADDA, H. ; TORRES, R. ; KAR, S. ; CLARKE, R. J. ; MUSGRAVE, I. O. ; NAJMUDIN, Z. ; BORGHESI, M. ; NEELY, D. ; MCKENNA, P. : Ion acceleration and plasma jet formation in ultra-thin foils undergoing expansion and relativistic transparency. In: *Nuclear Instruments and Methods in Physics Research, Section A: Accelerators, Spectrometers, Detectors and Associated Equipment* 829 (2016), 163–166. http://dx.doi.org/10.1016/j.nima.2016.02.032. – DOI 10.1016/j.nima.2016.02.032. – ISSN 01689002

[43] ALTENKIRCH, R. : *Holographic imaging and reconstruction of the structure of laser-induced modifications in thin films*, University of Rostock, Master's Thesis, 2021

[44] *Kapitel* 4,5. In: *Diffraction, Fourier Optics and Imaging*. John Wiley & Sons, Ltd. – ISBN 9780470085004, 41-83

[45] WIECHMANN, F.-E. : *Fokuscharakterisierung eines In-Line Holografie-Aufbaus*, University of Rostock, Bachelor Thesis, 2020

[46] WEINER, A. : *Zeitaufgelöste Abbildung von laserinduzierten Plasmen in dünnen Goldfolien*, University of Rostock, Bachelor Thesis, 2023

[47] COMFORT, J. R. AND DECKER, J. F. AND LYNK, E. T. AND SCULLY, M. O. AND QUINTON, A. R.: Energy loss and straggling of alpha particles in metal foils.

In: *Physical Review* 150 (1966), Nr. 1, 249–256. http://dx.doi.org/10.1103/PhysRev.150.249. – DOI 10.1103/PhysRev.150.249. ISBN 9780333227794

[48] SOGARD, M. R.: An empirical study of electron backscattering from thin films. In: *Journal of Applied Physics* 51 (1980), Nr. 8, S. 4417–4425. http://dx.doi.org/10.1063/1.328263. – DOI 10.1063/1.328263. – ISSN 00218979

[49] LIU, J. M.: Simple technique for measurements of pulsed Gaussian-beam spot sizes. In: *Opt. Lett.* 7 (1982), May, Nr. 5, 196–198. http://dx.doi.org/10.1364/OL.7.000196. – DOI 10.1364/OL.7.000196

[50] GOODMAN, J. W.: *Introduction to Fourier optics*. Roberts and Company publishers, 2005

[51] DEMASKE, B. J. ; ZHAKHOVSKY, V. V. ; INOGAMOV, N. A. ; OLEYNIK, I. I.: Ablation and spallation of gold films irradiated by ultrashort laser pulses. In: *Phys. Rev. B* 82 (2010), Aug, 064113. http://dx.doi.org/10.1103/PhysRevB.82.064113. – DOI 10.1103/PhysRevB.82.064113

[52] ZHOU, S. ; ZHAO, K. ; SHEN, H. : Ablation of gold film on different substrates by ultrafast laser. In: *Optics & Laser Technology* 132 (2020), 106495. http://dx.doi.org/https://doi.org/10.1016/j.optlastec.2020.106495. – DOI https://doi.org/10.1016/j.optlastec.2020.106495. – ISSN 0030–3992

[53] GUAY, J. ; VILLAFRANCA, A. ; BASET, F. ; POPOV, K. ; RAMUNNO, L. ; BHARDWAJ, V. : Polarization-dependent femtosecond laser ablation of poly-methyl methacrylate. In: *New Journal of Physics* 14 (2012), Nr. 8, S. 085010

[54] VENKATAKRISHNAN, K. ; TAN, B. ; STANLEY, P. ; SIVAKUMAR, N. R.: The effect of polarization on ultrashort pulsed laser ablation of thin metal films. In: *Journal of Applied Physics* 92 (2002), 08, Nr. 3, 1604-1607. http://dx.doi.org/10.1063/1.1487453. – DOI 10.1063/1.1487453. – ISSN 0021–8979

[55] GUIZAR-SICAIROS, M. ; FIENUP, J. R.: Understanding the twin-image problem in phase retrieval. In: *J. Opt. Soc. Am. A* 29 (2012), Nov, Nr. 11, 2367–2375. http://dx.doi.org/10.1364/JOSAA.29.002367. – DOI 10.1364/JOSAA.29.002367

[56] FIENUP, J. R. ; WACKERMAN, C. : Phase-retrieval stagnation problems and solutions. In: *JOSA A* 3 (1986), Nr. 11, S. 1897–1907

[57] RONG, L. ; LI, Y. ; LIU, S. ; XIAO, W. ; PAN, F. ; WANG, D. : Iterative solution to twin image problem in in-line digital holography. In: *Optics and Lasers in Engineering* 51 (2013), Nr. 5, 553-559. http://

dx.doi.org/https://doi.org/10.1016/j.optlaseng.2012.12.007. – DOI https://doi.org/10.1016/j.optlaseng.2012.12.007. – ISSN 0143–8166

[58] ITINA, T. E. ; HERMANN, J. ; DELAPORTE, P. ; SENTIS, M. : Laser-generated plasma plume expansion: Combined continuous-microscopic modeling. In: *Phys. Rev. E* 66 (2002), Dec, 066406. http://dx.doi.org/10.1103/PhysRevE.66.066406. – DOI 10.1103/PhysRevE.66.066406

[59] IONIN, A. A. ; KUDRYASHOV, S. I. ; SELEZNEV, L. V. ; SINITSYN, D. V. ; BUNKIN, A. F. ; LEDNEV, V. N. ; PERSHIN, S. M.: Thermal melting and ablation of silicon by femtosecond laser radiation. In: *Journal of Experimental and Theoretical Physics* 116 (2013), Nr. 3, S. 347–362. http://dx.doi.org/10.1134/S106377611302012X. – DOI 10.1134/S106377611302012X. – ISSN 10637761

[60] GARCIA-LECHUGA, M. ; SIEGEL, J. ; HERNANDEZ-RUEDA, J. ; SOLIS, J. : *Transient Newton rings in dielectrics upon fs laser ablation*. https://arxiv.org/abs/1405.5419. Version: 2014

[61] NISHIKINO, M. ; HASEGAWA, N. ; TOMITA, T. ; MINAMI, Y. ; EYAMA, T. ; KAKIMOTO, N. ; IZUTSU, R. ; BABA, M. ; KAWACHI, T. ; SUEMOTO, T. : Formation of x-ray Newton's rings from nano-scale spallation shells of metals in laser ablation. In: *AIP Advances* 7 (2017), 01, Nr. 1, 015311. http://dx.doi.org/10.1063/1.4975218. – DOI 10.1063/1.4975218. – ISSN 2158–3226

Selbstständigkeitserklärung

Ich versichere hiermit, dass ich die vorliegende Arbeit selbstständig verfasst und keine anderen als die angegebenen Quellen und Hilfsmittel benutzt habe. Ich versichere, dass die eingereichte elektronische Fassung mit den gedruckten Exemplaren übereinstimmt.

Rostock, (26.08.2024)